Fuel 357 (2024) 129949

Contents lists available at ScienceDirect

Fuel

journal homepage: www.elsevier.com/locate/fuel

Full length article

Effects of geological heterogeneity on gas mixing during underground hydrogen storage (UHS) in braided-fluvial reservoirs

Zhenkai Bo [a,*], Sebastian Hörning [a], Jim R. Underschultz [a], Andrew Garnett [a], Suzanne Hurter [a,b]

[a] Centre for Natural Gas, University of Queensland, St Lucia, Brisbane, 4072, Queensland, Australia
[b] TNO, Applied Geosciences, Princetonlaan 6, Utrecht, The Netherlands

ARTICLE INFO

Keywords:
Underground hydrogen storage
Gas mixing
Geological heterogeneity
Braided fluvial reservoirs
Reservoir simulation

ABSTRACT

Hydrogen, as an energy carrier, is at the centre of research attention for its potential advantages over electricity to transport and store excessive renewable energy at the GW scale as part of the energy transition. To store energy at such a large scale and in a seasonal manner, energy storage technologies such as compressed air storage and high-temperature aquifer thermal storage are proposed, where Underground Hydrogen Storage (UHS) in porous reservoirs may be an important technology for hydrogen economy. Research studies suggest the necessity of using alternative gas to hydrogen as cushion gas due to the very low density at reservoir conditions and the high production cost of hydrogen. In addition, the potentially lower development cost of UHS in existing depleted natural gas reservoirs or former sites for underground gas storage compared to that of saline aquifers makes gas mixing a real possibility for future UHS operations. However, this topic is rarely studied, let alone its geological governing factors. In this study, we focus on the most likely geological settings for early UHS projects (Depleted gas fields in high permeability braided fluvial reservoirs) to understand the potential impacts of geological heterogeneity on project economics.

To quantify the possible gas mixing induced by macro-scale heterogeneity and find the dominant factors that affect storage performance, in this study, we start by building synthetic high permeability water-gas reservoir model with geological characteristics of braided-fluvial systems often encountered in the oil and gas industry. Then we examine the effects of structural and litho-facies heterogeneity on gas mixing processes during typical UHS projects (10 mol% hydrogen-methane mixture as stored gas) via compositional numerical simulation. Homogeneous cases with different injection/production rates are also part of the sensitivity analysis. The cumulative days hydrogen fraction in produced stream is used as the metric for quantifying gas mixing during this process. Our results show that, compared to the homogeneous cases, macro-scale geological heterogeneity will intensify gas mixing and degrade the hydrogen fraction in the produced stream, affecting up to 15.8% of the recovery in 10 years (6% more than the homogeneous cases). Geological structure (reservoir dip angle and closure area) is a first-order determining factor above facies heterogeneity (braided channel dimensions). It determines the level of methane breakthrough during UHS projects in all the test cases, leading to contrasting gas mixing behaviors. Our study hereby provides a systematic method for evaluating gas mixing in UHS projects and facilitates future UHS techno-economic analysis.

1. Introduction

Hydrogen, as a low-carbon energy carrier and feedstock for chemicals, is currently the centre of attention to replace fossil fuels in energy supply while combating climate change [1–3]. For example, the power transmission capacity of a typical commercial transmission line is 2 GW, and a hydrogen gas pipeline can carry the equivalent of 10 GW or more [4], making hydrogen potentially suitable for being transported from a renewable-energy-rich area such as the ocean or desert to a population-dense region [5]. Green hydrogen has been proposed to be produced on the order of 14 Mt/year from renewable energy powered electrolysis technology [6], and blue hydrogen aims to be produced on 10 Mt/year from fossil fuel coupled with carbon capture and storage [7,8]. Depending on the available resources and potential role in the future international hydrogen market, countries are considering different scenarios to decarbonize their energy mix with the inclusion of hydrogen [9,10], or to supply hydrogen to energy-importing countries [11]. In both cases, large-scale hydrogen storage facilities will be essential [12–14] and underground hydrogen storage

* Corresponding author.
E-mail address: z.bo@uq.net.au (Z. Bo).

https://doi.org/10.1016/j.fuel.2023.129949
Received 7 June 2023; Received in revised form 6 September 2023; Accepted 25 September 2023
Available online 5 October 2023

is the only known hydrogen storage technology that can be used to achieve a potential power output of 0.4 GW for salt cavern and up to 1 GW for depleted oil and gas fields [15].

The purpose of Underground Hydrogen Storage (UHS) is to store excess energy as hydrogen in subsurface structures during energy production peak periods, and to withdraw it when energy demand is high and/or energy production is low [16,17]. Although there are decades of UHS experience in utilizing salt caverns [18], their relatively small storage capacity and the limited geological availability of salt formations over large geographical areas have led to recent feasibility investigations of UHS in porous reservoirs which are still largely unstudied [19]. Researchers from Australia, China, Germany, Poland, U.K., and U.S. have summarized the challenges of implementing UHS on a larger scale. Their findings can be distilled into specific aspects: high cushion gas requirement due to the low molecular weight of hydrogen [15,20], hydrogen loss due to gas diffusion and mixing [13,20,21], well integrity issues due to potential hydrogen embrittlement [22–24], hydrogen loss due to abiotic and biotic chemical reactions [10,25–27], a lack of business case demonstration and uncertain public acceptance [19]. In response to these challenges, research regarding feasibility in terms of geological resources [9,10,28,29], effects of wettability on flow [30–32], operation management and storage capacity [33,34], and risk posed by abiotic geochemical reactions [22,25,35], biotic reactions [36,37], and well integrity [24] have been investigated during the most recent few years. However, despite efforts that have been put into this emerging technology, based on the latest research findings [19,38,39], there are still uncertainties and risks to address before the successful implementation of UHS in porous reservoirs.

At this stage of UHS technology deployment, also driven by immature hydrogen production from renewable energy technologies [40,41], the UHS storage demand is not projected to be more than 100,000 tonnes domestically by 2040 in Australia [42]. Hence, hydrogen-methane mixtures (blend) are being used to conduct pilot UHS field tests [14]. For such UHS projects in depleted gas reservoirs, a commonly used hydrogen fraction in the stored fluid is 10% [14], given potential well integrity issues when the hydrogen fraction is over this value [43]. Moreover, various alternative gases may be more suitable cushion gas for UHS than pure hydrogen, e.g. nitrogen [34,44]. Therefore, it is likely to see hydrogen mixing with other gases during future UHS projects.

However, mixing hydrogen with cushion gas, which is initially only hydrocarbon gas during UHS in depleted gas reservoirs, can cause problems. Some critical minerals, e.g. pyrite, anhydrite, and calcite might trigger major biotic and abiotic hydrogen-consuming processes such as methanogenesis, sulfate reduction, and acetogenesis [26,37], affecting the hydrogen fraction in the produced stream. Pipeline transport as well as the final use (e.g. fuel cell) of hydrogen or hydrogen-methane mixtures imposes strict specifications and constraints on the composition of the product [45,46]. If the hydrogen fraction is below a certain threshold, the utilization of produced hydrogen gas can be affected and expensive surface separation facilities may be required as a result [47]. Therefore, many reservoir-scale UHS simulation studies report the hydrogen fraction in the produced stream in addition to hydrogen recovery [34,48–50]. In 2016, the H2STORE project conducted a UHS reservoir simulation of 5 years' cyclic operation with an injection of pure hydrogen into a reservoir with nitrogen and methane. They reported that the hydrogen fraction in the produced stream would decrease from 100% to 80% during the simulation of production and then increase over 5 cycles to 85% [48]. Lysyy et al. [34] investigated the most suitable zone (water, oil or gas) for storing hydrogen in a model of Norne field [34]. The production stream included up to 100% hydrogen fraction; this might be because of the large amount of hydrogen injected initially as cushion gas. As they reported, hydrogen recovery was only around 14% and the hydrogen fraction decreased to between 70 and 80% when hydrogen recovery increases between 50% to 58% due to less injected hydrogen acting as cushion gas [34]. Similar hydrogen recovery ranged, from 32% to 66% during cyclic operation, are reported when investigating suitable cushion gas types in a partially depleted gas reservoir [44]. In summary, studies have shown various influences on the hydrogen fraction in the produced stream under different injection/production scenarios. The aim of this study is to extend this investigation to a geological context.

The injection of hydrogen in porous reservoirs with residual methane as a cushion gas represents a miscible displacement process as a gas phase while it is an immiscible flooding process in the presence of gas and water [51]. Meanwhile, porous reservoirs can be naturally heterogeneous at several scales, and need parameters at multiple levels to be characterized [52–54]. Among these geological levels, unless the miscible gas flow is solved at the pore-scale [55,56], advection is represented with a mean gas flux over a volume, and the fluctuation with respect to this mean gas flux (dispersion) across the simulation domain results in gas mixing [57]. Given that heterogeneity occurs at all scales [57,58], preferential flow paths for advection, e.g. channeling flow at reservoir-scale [59,60] will intensify such fluctuation, as well as the gas mixing. Thus, it is reasonable to expect that spatial variation of geological properties (heterogeneity) will impact the gas mixing, as well as the subsequent hydrogen fraction in the produced stream and its recovery [54,59]. Knowing those effects could help in the design of the development strategy for a UHS project and provide valuable insight for future business cases. Reservoir structure variation such as reservoir dip will have significant impact on the injectivity and productivity of UHS in both depleted gas reservoirs [61] and saline aquifers [62]. It has been reported that when the reservoir is permeable enough (permeability above 200 mD), a reservoir dip ranging between 5 to 15° is reported as the optimal angle for UHS [61]. However, these studies focus on UHS productivity and hydrogen recovery in homogeneous reservoir models, and the effects of geological heterogeneity on hydrogen gas mixing and subsequent hydrogen fraction in the produced stream are yet to be investigated [10,62].

The aim of this study is to investigate the influence of geological parameters for the hydrogen gas mixing processes during UHS. In particular, the author focuses on braided-fluvial reservoirs as they can make excellent, productive reservoirs with great lateral continuity [63]. This study investigates the hydrogen fraction in the produced stream during production periods of an underground hydrogen-methane mixture storage project that injects a constant hydrogen-methane mixture with 10 mol% hydrogen following current industry practice. First, synthetic reservoir models that represent braided-fluvial geological settings are built. Then, we perform a series of numerical simulations to study how, under the same productivity and injectivity, the resulting hydrogen fraction in the produced stream is affected by reservoir structure, fluvial channel dimensions, and variable injection/production rates. In each simulation, the hydrogen fraction during the production period is recorded, and the periods at which it drops below a specified value can be observed. Our results show that even under the same cyclic injectivity and productivity, geological heterogeneity can have significant effects on the resulting hydrogen fraction in the produced stream, leading to distinct economic and technical UHS performance differences between reservoirs of braided-fluvial systems.

2. Methodology

This study relies on reservoir simulations to investigate the impact of the geological characteristics of a storage reservoir on gas mixing and the resulting variation of the hydrogen fraction in the produced stream in a cyclic hydrogen-methane mixture storage scenario. First, the characteristics of braided-fluvial systems are discussed and we present how they are realized in two distinct geological structural models. There are two heterogeneity scales (on top of structure) to these models: (1) the lithological makeup and geometrical distribution of permeable sand bodies in a matrix of less permeable shaly sediments and (2) the distribution of porosity and permeability within the lithological bodies

that are due to smaller scale variations in porosity and permeability as can be derived from the integration of rock core measurements and geophysical log interpretation (petrophysical model). The statistical characteristics of these variations are used to populate the properties of each litho-facies in the geological model. Finally, reservoir simulations setup of simple cyclic injection and production scenarios are described.

2.1. Braided-fluvial system sediments

The unique depositional pattern of braided channels was recognized in the nineteenth century, but the first attempt to differentiate it from a meandering-fluvial system was not made until 1962. While meandering rivers show regular and continuous runoff along mostly single channels [64], the braided river system exhibits annually intermittent discharge of enormous amounts of water, causing devastating effects. Several conditions including extreme precipitation, sparse vegetation, and steep slopes cause differences between meandering and braided rivers' sediment deposition and the resulting stratigraphic architecture. Later, [65] developed four facies models for braided rivers. Sand bar morphology and grain size distribution differentiate braided rivers from other types that have gravel bars with common longitudinal and linguoid shapes. In another work focusing on facies models of fluvial systems [66,67] describe the bulk deposit from braidplains as mostly gravel bedforms (95% of thickness) with thin sand sheets due to cross-cutting between numerous broad low-sinuosity river channels. These facies models become a set of architectural schemes for describing fluvial systems [67]. Until recently, Gibling argued that although there have been extensive studies of the internal architecture of channel deposits, only a few deals with their dimensions and external geometry [68]. Thus, Gibling [68] assembled a database of more than 1500 examples of channel-fill deposits, ranging in age from Precambrian to Quaternary. In this database, Potter's terminology [69] is used for defining architectural elements developed by vertical stacking and lateral amalgamation of channel bodies. A similar system was used to develop a database for quantitative facies modeling by Colombera et al. [70]. These aforementioned achievements provide valuable geological insights for the high-fidelity modeling of braided-fluvial system reservoirs.

2.2. Braided-fluvial reservoirs in oil and gas industry

Braided-fluvial systems make excellent, productive oil and gas reservoirs [63]. Typical examples include Prudhoe Bay, Alaska, U.S., Cooper Basin, Australia, Murdoch Sandstone, North Sea, U.K., and Precipice Sandstone, Surat Basin, Australia [71–73]. These reservoirs show sand-sheet geometry originated from broad braidplains [67]. Sand-sheet reservoirs and braidplains reflect high relief of the source-area and steep paleoslopes [67]. However, it does not mean that all the braided-fluvial reservoirs result from steep reservoir dips and complex strain, as structural heterogeneity can be generated from syn and post-depositional activities such as regional uplift or subsidence, faults, folds, and salt diapirs [74]. Therefore, braidplain strata can have low [75] or high [76] dips and also be compartmentalized into small [71] or large [75,77] production blocks.

Another typical characteristic of braided-system reservoirs is the high sand-to-gross ratio, usually between 85% to 95% [71,75,78]. In addition, well logs commonly show quartz-dominant fining-upward packages from coarse-grained conglomerates to fine-grained sandstones, to finally trace amounts of mud breccias [75,78]. These observations are consistent with the braided system facies models built by Miall [65,67]. Depending on the rock structure, conglomerates may or may not be as permeable as sandstones [79]. Consequently, during the modeling process of braided-fluvial reservoirs, the system is often simplified into two categories of flow unit (flow or non-flow), made up of predominantly two rock types (sandstone and claystone) [72,80].

2.3. Generic braided-fluvial reservoir modeling

Based on the characteristics of braided-fluvial reservoirs introduced earlier, we chose to model two types of reservoir structures in our generic braided-fluvial reservoir models. They are defined as type 1 and 2 structures, representing braided-fluvial reservoirs with different post-depositional deformation. In this study, 4 simulation cases are designed for each type of structure, making a total number of 8 simulation cases. Among them, cases 1 to 4 are designed for the type 1 structure, and cases 5 to 8 are designed for the type 2 structure. Within each group of simulation cases, the same four cases are modeled to include
(1) a homogeneous case for uniform permeability and porosity of a single litho-facies;
(2) a heterogeneous case with small channel body geometry populated by two litho-facies with variable permeability and porosity;
(3) a second heterogeneous case with a large channel body geometry populated by two litho-facies with variable permeability and porosity;
(4) a homogeneous case (same as scenario 1) but with an alternative injection/production rate.

The type 1 structure, used for cases 1, 2, 3, and 4, is designed to model braided-fluvial reservoirs in a dome structure with gentle dip (3.57°) and a large production area (2.56 km^2). The gross formation thickness is 40 m and is at a depth of 1500 m. A reservoir pressure of 15030 kPa (from field data) and a temperature of 58.5 °C (from Fenton Creek field, see the type 2 structure) are set at the original water-gas contact [76]. The model is discretized into $40 * 40 * 10$ grid blocks with grid size $40 * 40 * 1.75$ m. The top boundary is closed representing the regional unbroken low-permeable shale (sealing) unit, while the lateral and bottom boundaries are open and connected to aquifers. Fig. 1(a) shows the contour map of the type 1 structure.

The type 2 structure, used for cases 5, 6, 7, and 8, is designed to model braided-fluvial reservoirs in a fault-bounded anticline with steep dip (14°) [71] and a small production area (0.64 km^2). The formation thickness is 60 m. Same as the type 1 structure, the reservoir is at a depth of 1500 m and the reservoir pressure at the original water-gas contact is 15030 kPa (from field data), as well as the reservoir temperature [76]. To keep the grid size of the two types of models consistent, type 2 structure models are discretized into 60*18*30 grid blocks, of which 20500 are active. The top and lateral boundaries are all closed, only the bottom boundary is open with aquifer support. Fig. 1 (b) shows the contour map of the type 2 structure. It is noteworthy that the model in Fig. 1 (b) is based on the open-source Fenton Creek depleted gas reservoir model. This gas field reservoir was deposited in a high-energy fluvial environment with a high sand-to-gross ratio (around 80% to 90%) [76]. The initial water-gas contact depth is set such the initial gas in place for both types of structures ($1.062 * 10^8$ m^3 at surface conditions) is the same. Finally, the original production well Fenton Creek-1 is located northeast down-dip to the crest of the reservoir with a 200 m offset. To produce the stored hydrogen-methane gas mixture from the top of the crest, both the injection well and production well are put at the location of well 'INJ' in Fig. 1.

The facies model for the base case of types 1 and 2 (cases 1 and 5) is homogeneous with 100% sandstone, as well as for cases 4 and 8. Cases 2, 3, 6, and 7 use an object-based simulation algorithm in the commercial geological modeling software Petrel™ (SLB) [81] to populate sandstone channels on a background of claystone [82]. Two channel body geometries are tested: small channel dimension (cases 2 and 6) and large channel dimension (cases 3 and 7) [71,76]. They differ from each other in channel amplitude, wavelength, width, and depth. Table 1 provides an overview of the characteristics of the simulation cases. Channel dimension values in Table 1 come from analogous braided-fluvial reservoir modeling studies [72], a braided river dimension database [68,70], and modern analogs [83]. To take the uncertainty of the stochastic simulation during object-based and Sequential Gaussian Simulation (for porosity) into account, 100 stochastic realizations of cases 2, 3, 6, and 7 were created through varying the simulation seeds in Petrel™ (geo-statistics input were kept the same). Fig. 2 shows examples of populated facies map out of small channel dimension (Fig. 2 a)), and large channel dimension (Fig. 2 (c)).

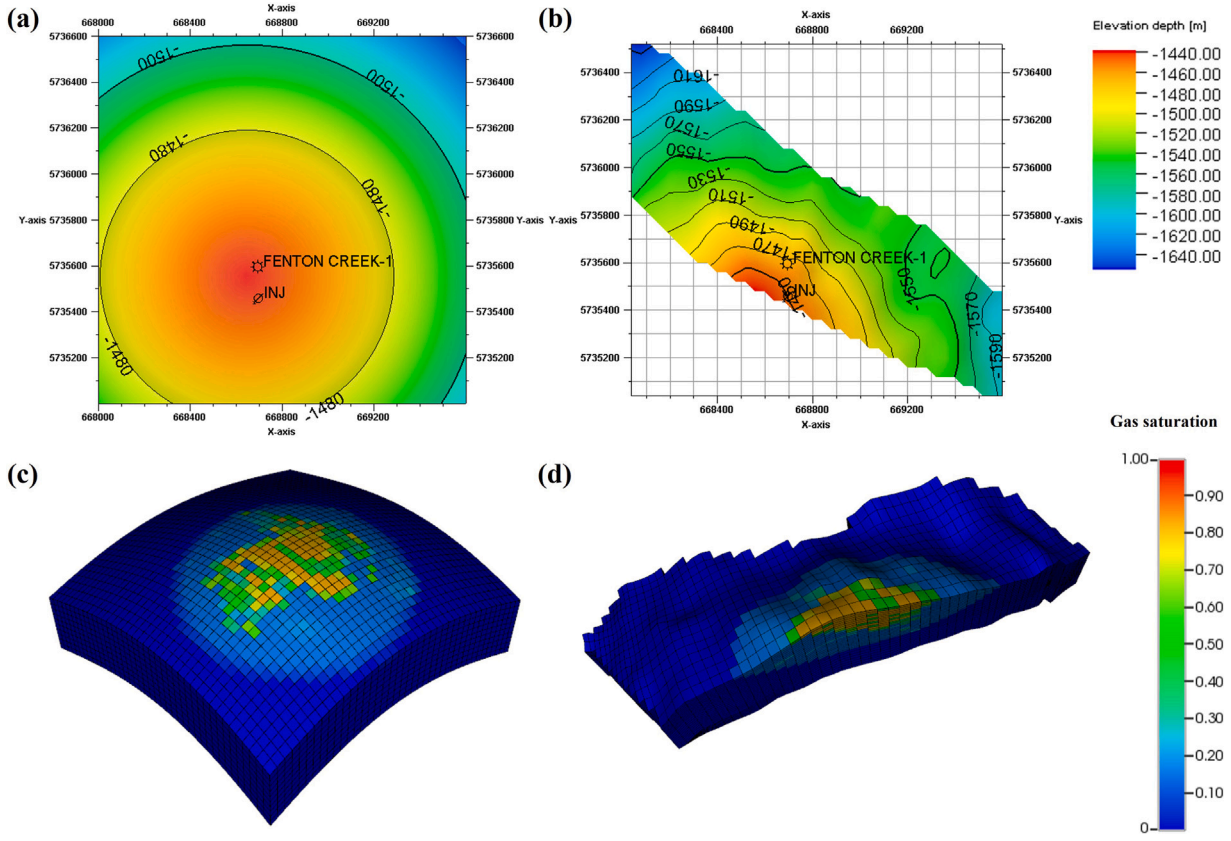

Fig. 1. (a) Contour map of type 1 structure, an open dome structure with small dip; (b) contour map of type 2 structure, a closed fault-bounded anticline structure with steep dip; (c) Methane-brine saturation map in 3D after primary production of a heterogeneous case; (d) Methane-brine saturation map in 3D after primary production of a heterogeneous case.

Table 1
Overview and description of each testing case.

Case	Facies heterogeneity	Channel amplitude (m)	Channel wavelength (m)	Channel width (m)	Channel depth (m)	Inj/Pro rate ($*\ 10^6 m^3/day$)
			Type 1 structure models			
1	Homogeneous	–	–	–	–	0.35
2	Heterogeneous (100 realizations)	100	300	19	5	0.35
3	Heterogeneous (100 realizations)	500	6000	150	5	0.35
4	Homogeneous	–	–	–	–	0.7
			Type 2 structure models			
5	Homogeneous	–	–	–	–	0.35
6	Heterogeneous (100 realizations)	100	300	19	5	0.35
7	Heterogeneous (100 realizations)	500	6000	150	5	0.35
8	Homogeneous	–	–	–	–	0.7

2.4. Petrophysics modeling

The petrophysical modeling for both types of structure (type 1 and 2) uses the same data (well data from the Fenton Creek field [84]) and algorithm (Sequential Gaussian Simulation [82]). For the heterogeneous cases (2, 3, 6, and 7), the well porosity data are first upscaled (volume-weighted arithmetic) and input into the structure models (see Fig. 1) at corresponding depth and location, then Sequential Gaussian simulation is performed based on well data and the variogram of each field. Finally, porosity-permeability transformation functions from the Fenton Creek field are used to translate the simulated porosity models into permeability models. Therefore both the porosity and permeability fields show the same pattern and scale of heterogeneity. Table 2 provides the statistics used for populating porosity and porosity-transformation functions for sandstone and claystone facies: the average permeability is around 660 mD and the average porosity is 0.143 which is used for the property models of homogeneous cases in Table 1. Fig. 2 (b) and (d) shows the areal view of permeability fields resulting from facies maps of figure (a) and (c).

Capillary pressure and relative permeability data (air-brine system, including imbibition) are available from the core analysis [84]. Fig. 3 shows the relative permeability models for sandstone and claystone facies used in this study. In this regard, we are using the methane-brine relative permeability (comparative to the air-brine relative permeability [85]) as the proxy for both the pure methane and hydrogen-methane mixture-brine relative permeability. The reason for this is twofold. One is that the hydrogen fraction in the study is as low as 10 mol%. This percentage of hydrogen will not considerably vary the fluid dynamics

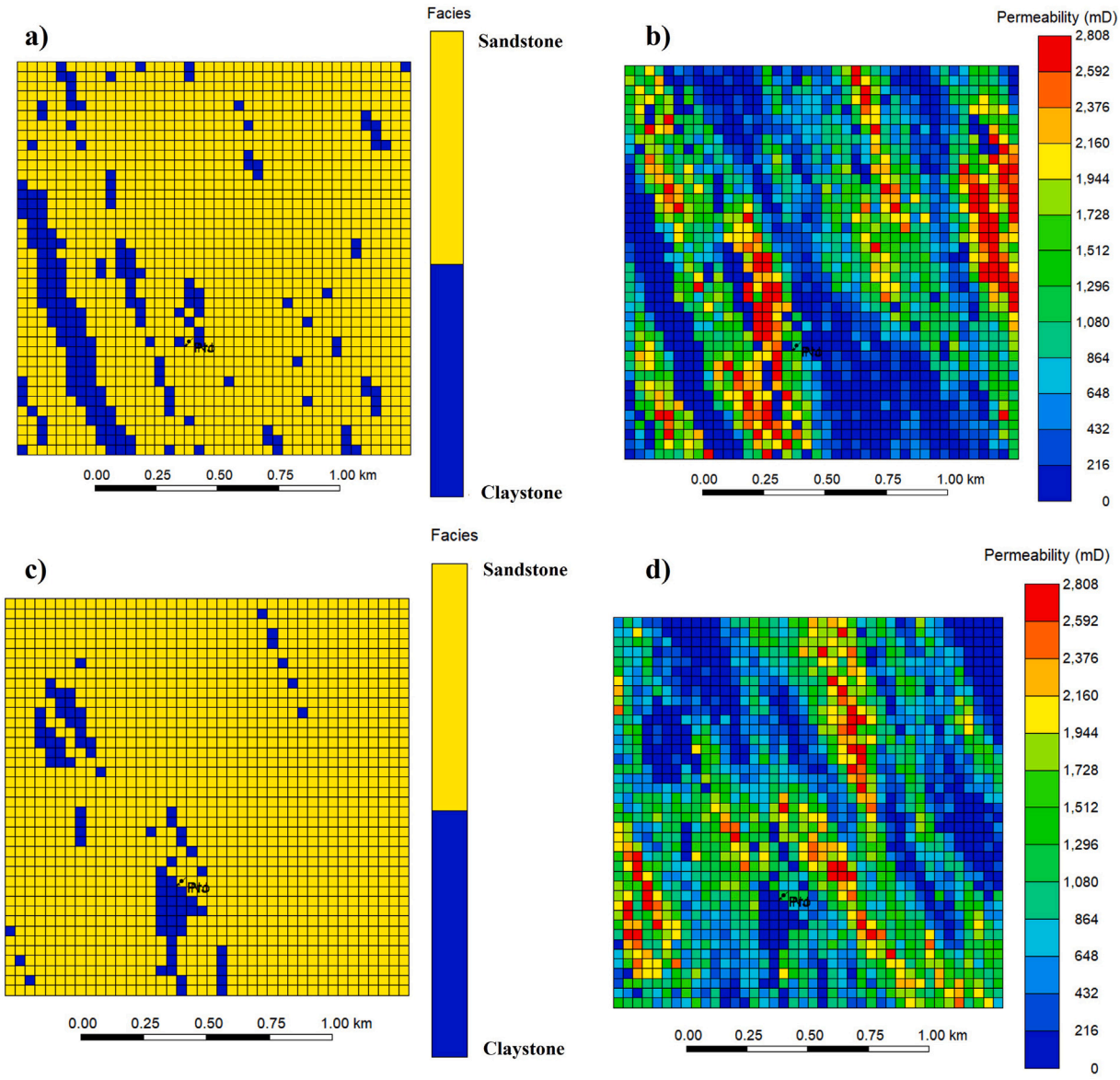

Fig. 2. Examples of an areal view of facies and permeability distributions (all from the second layer of the model). (a) Facies distribution (object-based simulation) for a small channel in a type 1 structure, the (blue) claystone facies is fairly scattered over the domain but includes several continuous features; (b) Permeability distribution of a), high permeability channels alternate with low permeability units, i.e. strong heterogeneity producing narrow flow paths; (c) Facies distribution (object-based simulation) for a large channel in a type 1 structure, the claystone facies appears as fairly isolated 'islands'; (d) Permeability distribution of (c), high permeability channels are well connected allowing flow over broad areas with islands of low permeability. (For interpretation of the references to color in this figure legend, the reader is referred to the web version of this article.)

Table 2
Statistics for Sequential Gaussian Simulation of porosity models and porosity-permeability transformation functions of sandstone and claystone facies [84].

Facies	Variogram major range (m)	Variogram minor range (m)	Porosity output range (-)	Porosity-permeability transformation function
Sandstone	1000	200	0.057–0.25	$k = 1014 * 10^2 * \frac{\phi_e^3}{(1-\phi_e)^2}$
Claystone	2000	1000	0.035–0.12	$k = 1014 * 1.5^2 * \frac{\phi_e^3}{(1-\phi_e)^2}$

k is permeability; ϕ_e is effective porosity

compared to that of pure methane. For reference, the viscosity and density for pure methane, pure hydrogen, and hydrogen-methane mixture (10 mol% hydrogen) at the average reservoir temperature (58.5 °C) and pressure (12500 kPa) in our study are 83 kg/m^3 and 0.0153 cP, 8.44 kg/m^3 and 0.0097 cP, and 72.99 kg/m^3 and 0.0151 cP, respectively. The other is that the latest measured pure hydrogen-brine relative permeability models present unique characteristics of lower gas relative permeability and more severe hysteresis compared to that of other fluid systems. These mechanisms are not yet fully understood [38,86–88]. Hence, models describing the relative permeability of the hydrogen-methane mixture are not currently available. Further discussion on the potential impact of the relative permeability of the hydrogen-brine

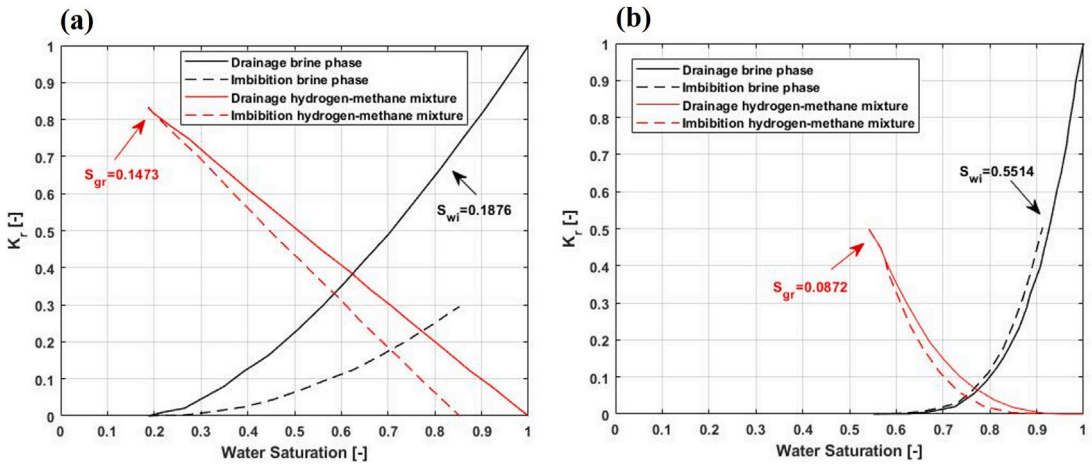

Fig. 3. (a) Sandstone facies relative permeability model from the fields; (b) Claystone facies relative permeability model from the fields; S_{wi} is the initial water saturation; S_{gr} is the residual gas saturation.

system and future work can be found in our previous work [88]. Capillary heterogeneity is considered through a Leverett J function which is routinely used [76,89], as Eq. (1).

$$P_c = J(S_w)(\frac{K}{\phi})^{0.5} \tag{1}$$

where $J(S_w)$ is a normalized capillary pressure function of water saturation from the fields [76]. Finally, capillary pressure hysteresis is not considered in this study as the scale of reservoir simulation is much larger than the characteristic capillary dimension [90] and related experimental hysteresis capillary pressure data (the air-brine data from the fields) are not available [84,88].

2.5. Simulation setup

During the reservoir-scale numerical simulation, there are several assumptions made for efficient simulation performance. It is assumed the reservoir matrix consists only of sandstone and claystone which is geochemically inactive in a hydrogen-brine-rock system [25]. No micro-organisms are presented in the reservoir simulation and no solubility is modeled, given the low solubility of hydrogen [25,91]. Methane is used here as a proxy for hydrocarbon gas in depleted gas reservoirs which could have other gas components. Moreover, Hydrogen and the hydrogen-methane mixture is assumed to be water-wet in the gas-brine-rock (sandstone and claystone) system based on experimental observations [51]. The dispersivity is set to 0 in all the cases to only account for heterogeneity-induced gas mixing [92]. A sensitivity study on dispersivity, numerical dispersion, and grid size (given the coarse grid size) was also conducted and the results are presented in Appendix. The simulations are performed using the compositional simulator CMG-GEM [93].

There are three stages in our simulation, (1) primary production of methane from the reservoir to reach the historical gas recovery of the fields [76], (2) initial injection using a hydrogen-methane mixture with 10 mol% hydrogen, followed by (3) 10 cyclic operations. The period of each cycle is 1 year for all the cases. Two injection/production schemes are used and the same total volume of injected/produced hydrogen is maintained in all cases. In the first '6 month' scheme, a hydrogen-methane mixture is injected for six consecutive months and then produced for the next six months and this is repeated for 10 years. The second is the '3 month' scheme with injection (the same hydrogen methane mixture) for 3 months, shut-in for 3 months, production for 3 months, then shut-in for another 3 months and this is repeated for 10 years. If the injection/production rate is doubled, the '6 month' scheme will change to the '3 month' scheme to make the total volume of injection/production consistent. Note that in Table 1, given that cases 4 and 8 use doubled injection/production rate compared to other cases, the injection/production scheme of them would be '3 month'. All the other cases will use the '6 month' injection /production scheme.

The simulation schedule and injection/production rate are set based on production history and simulation scenarios from the Feton Creek depleted gas reservoir modeling studies (injection/production rate ranges from $0.35 * 10^6$ m^3/day to $0.7 * 10^6$ m^3/day) [76]. These injection and production periods are longer than those used in other UHS reservoir simulation studies [34,44,48] in order to better compare and contrast the cases. Also, all tested cases use the same pressure constraints at the wells. For the purposes of this paper and simulation, the maximum bottom hole pressure for the injection well is set to 15000 kPa to assure that reservoir pressure does not exceed the initial (was 9662 kPa after the gas primary production stage) reservoir pressure, and the minimum bottom hole pressure for the production well is set to 5000 kPa to maintain the minimum pressure required for transportation and processing downstream [76].

3. Results and discussion

3.1. Homogeneous cases

Differences in structural style will affect the gas saturation and hydrogen fraction distribution even in homogeneous reservoir cases where uniform displacement is expected [48]. Cases 1 and 5 are designated to be the base case of type 1 and 2 structures, respectively. In the following, the results from these 2 cases are presented and the effect of differences in structural style is analyzed.

Case 1 simulates the storage of the hydrogen-methane mixture in a homogeneous slightly dipping dome structure (type 1 structure) where injection and production happen at the crest of the dome. As a result, the overall plume geometries of gas saturation and hydrogen fraction by the end of the 10th cycle are circular with a centre at the well location, as shown in Fig. 4. With the increasing number of cyclic operations, the fraction of gas in the reservoir approaches the composition of the injected fluid (10 mol% hydrogen). Hydrogen fraction is the highest down-dip of the reservoir (central right bottom corner of the gas cap, see Fig. 1) at the end of the production periods of each cycle. This is the exact opposite of the distribution of the high gas saturation area which is located at the top of the reservoir (central left top corner of the gas cap, see Fig. 1). The reason for this is that during the production period, viscous force plays the dominant role. As a result, residual methane gas residing at the bottom of the gas cap tends to break through and be produced from the top of the reservoir. From the right most diagrams of Fig. 4, this residual methane gas plume is not

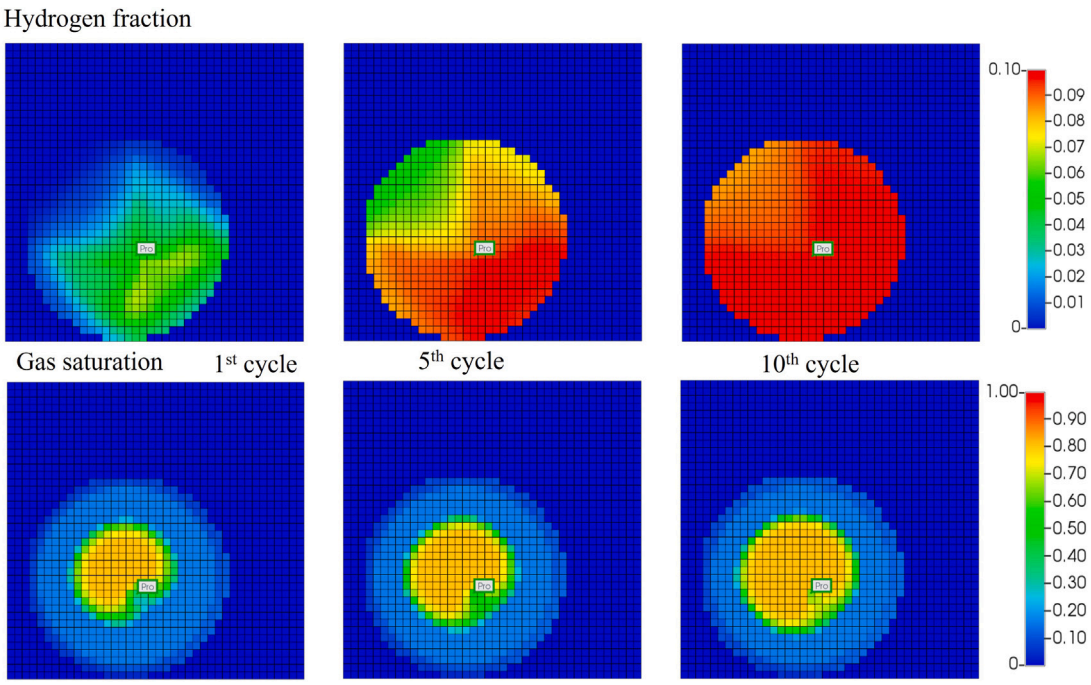

Fig. 4. Case 1 (homogeneous) map (areal) views on the top layer at the end of specified cycles. Top row: hydrogen fraction distribution map; Bottom row: gas saturation distribution map, the lighter blue color represents residual methane (gas) saturation at about 0.15; left: 1st cycle; middle: 5th cycle; right: 10th cycle. (For interpretation of the references to color in this figure legend, the reader is referred to the web version of this article.)

completely produced at the end of the 10th cycle and a certain portion of the gas cap still has a hydrogen fraction around 0.08, affecting the hydrogen gas fraction in the produced stream.

The situation in case 5 is different. Case 5 simulates the underground hydrogen-methane mixture storage in a fault-bounded anticline with homogeneous properties and a large dip (type 2 structure). Similar to case 1, injection and production also happen at the top of the reservoir. Fig. 5 shows the resulting hydrogen fraction and gas saturation distribution maps along a vertical section through the model. Since the surrounding boundaries are sealed by faults, the geometry of the gas cap is dictated by the geometry of the reservoir formation. Consistent with case 1, the hydrogen fraction is also generally independent of gas saturation. In addition, due to the breakthrough of residual methane gas, the hydrogen fraction is lower at the top of the reservoir at the end of the production period of the 1st and the 5th cycles (top and bottom column of Fig. 5). Better vertical displacement of the type 2 structure leads to the hydrogen fraction in the gas cap reaching nearly the same as that of the injected fluid (10 mol% hydrogen-methane mixture). In other words, residual pure methane is nearly completely produced by the end of the 10th cycle which will make the hydrogen gas fraction in the produced stream very close to that of the injected stream.

The two different gas distribution patterns in cases 1 and 5 resulting from different structures will cause different hydrogen fractions in the produced stream. Fig. 6 a) shows the hydrogen fraction in produced stream profiles in all 10 cycles where (b), (c), and (d) show the profiles in 1st, 5th, and 10th cycle, respectively (for reference, we also plot the average reservoir pressure and the cumulative hydrogen/methane production in appendix, see Fig. 17). Compared to Fig. 6 (b), (c), and (d), it is clear that the hydrogen fraction of the produced stream is becoming close to that of the injected stream which is consistent with the increasing hydrogen fraction in Figs. 4 and 5. Although case 1 and case 5 are very similar in Fig. 6 a), the difference between them is 25% in terms of hydrogen fraction at the end of the 1st cycle. Moreover, from the 1st to 10th cycle, the hydrogen fraction of case 1 always decreases faster than that of case 5. This can be explained with Figs. 4 and 5: the type 1 structure (case 1) has a larger area and less vertical displacement. In this study, the only driving mechanisms considered are gravity, capillary, and viscous forces, respectively. Therefore, the hydrogen concentration of a grid block in the model is a hyperbolic function of the volume of fluids flowing through the pore space in the grid block. From this perspective, the flow paths in the two types of structure (cases 1 and 5) will determine how the fluids at each point of the model flow back to the production well and how the resulting gas mixing induces hydrogen fraction variation. As a result, in Fig. 6 (b), (c), and (d), the hydrogen fraction of case 1 is always higher than that of case 5 during early production periods then quickly drops below it (flow paths do not change).

The gas mixing is severe (Fig. 6) during the first several cycles and the hydrogen fraction can drop below 0.05 which is half of that in the injected stream. Such results might disturb a UHS operation or require gas processing on the surface, causing a negative influence on the economics of UHS projects. To quantify this negative influence brought by geological heterogeneity, we set a hydrogen fraction of 0.09 as a specification below which extra loss may occur and count the cumulative days of each case in which the hydrogen fraction drops below this value. The value 0.09 has been marked in Fig. 6 with a dot-dash line and one can find a considerable fraction of production periods that exhibit hydrogen fraction below 0.09. Fig. 7 shows the cumulative days for which the hydrogen fraction drops below 0.09 at the end of each cycle in cases 1 and 5. Overall, the cumulative days increase with the number of cycles and the final cumulative days of cases 1 and 5 are 159 and 179, respectively. This means for homogeneous cases presented here, 8.7–9.8% of recovery would be affected by gas mixing. As discussed before, the type 2 structure shows a stronger vertical hydrogen displacement and produces most of the residual pure methane. Consequently, the cumulative days of case 5 are larger than case 1 from the first cycle and are 12.6% more at the end of 10 cycles. Although case 1 still has residual methane breaking through during production at the end of the 10th cycle, the type 1 structure has potentially lower gas processing costs given this current hydrogen fraction specification. In contrast, from Fig. 7, the stronger vertical displacement of the type 2 structure results in a quicker production of residual methane and subsequently fewer cycles are required to achieve a stable hydrogen fraction (days below 0.09 is stable since 3rd

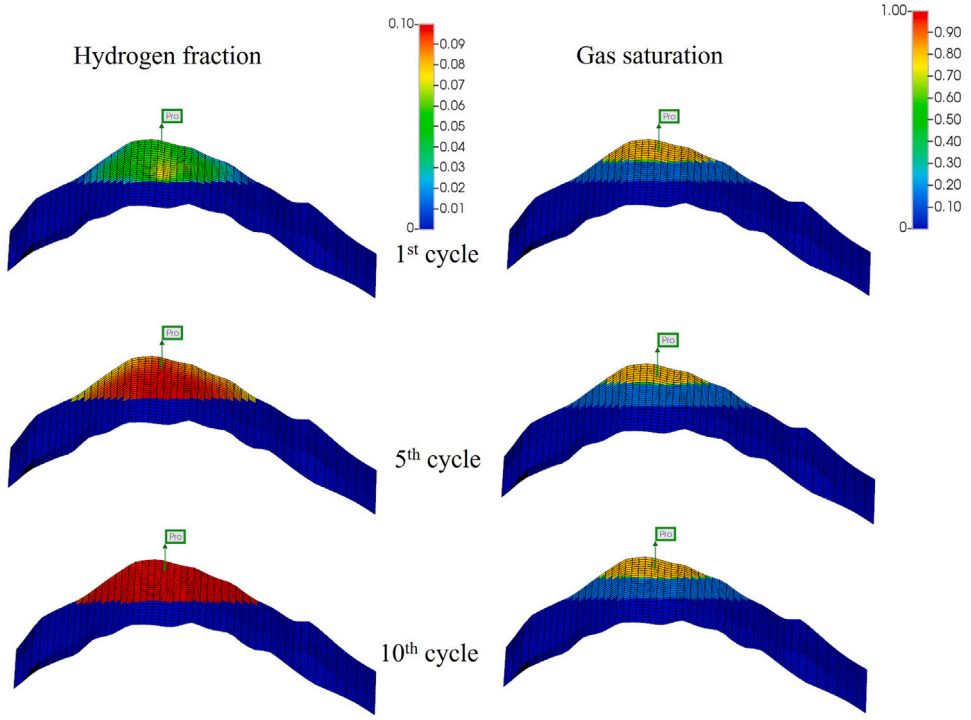

Fig. 5. Case 5 (homogeneous) vertical sections through the well. Left column: hydrogen fraction distribution map; Right column: gas saturation distribution map; top: 1st cycle; middle: 5th cycle; bottom: 10th cycle.

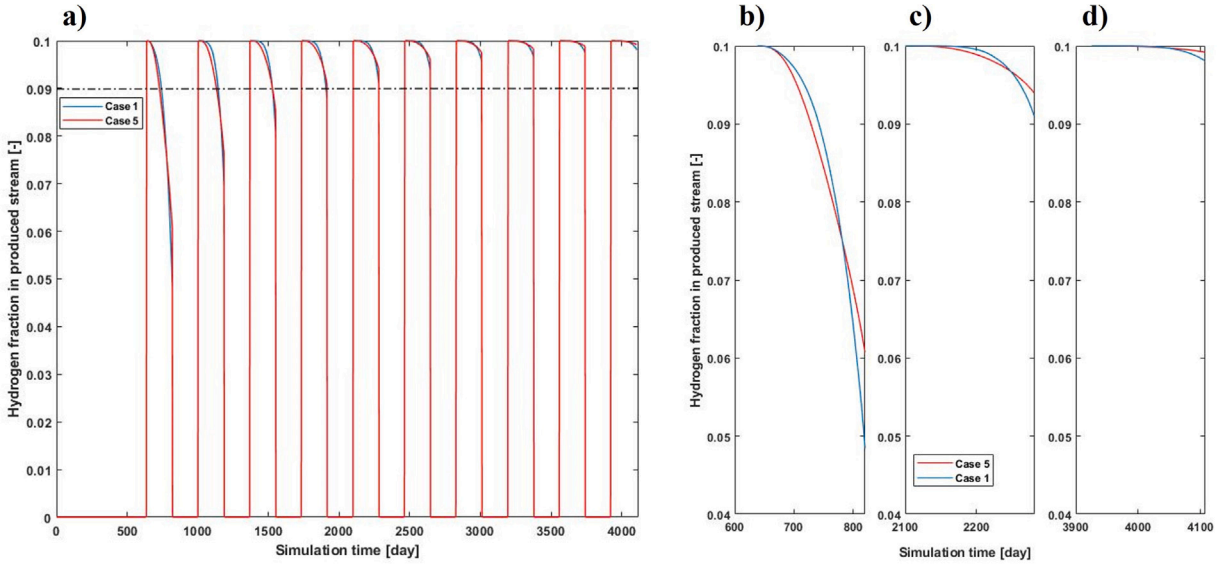

Fig. 6. Hydrogen fraction in produced stream profiles over time of case 1 (blue) and 5 (red): (a) profiles of all 10 cycles. The dot-dash line marks the specified value 0.09; (b) profiles of 1st cycle; (c) profiles of 5th cycle; (d) profiles of 10th cycle. (For interpretation of the references to color in this figure legend, the reader is referred to the web version of this article.)

cycle, compared to 4th cycle in case 1). Moreover, the type 2 structure delivers a higher hydrogen fraction by the end of each cycle (Fig. 6). This is an advantage over the type 1 structure when the requirement is strict (i.e. when pure hydrogen instead of a hydrogen-methane mixture is cycled).

3.2. Heterogeneous cases

Cases 2/3 and 6/7 are designed to investigate the effects of heterogeneous litho-facies distributions in braided-fluvial systems on the displacement behavior of hydrogen-methane mixture storage and resulting gas mixing in the subsurface. Among them, cases 2 and 6 contain a facies distribution originating in small channel bodies, while cases 3 and 7 have a facies distribution originating in large channel bodies. To account for geological uncertainty, each case is modeled with 100 stochastic realizations. First, the authors present the results of the P50 realization of each case in terms of cumulative days of hydrogen fraction less than 0.09. Then, the P10, P50, and P90 results are reported.

A heterogeneous facies distribution leads to distinct hydrogen fraction and gas saturation distribution during cyclic operations. Fig. 8

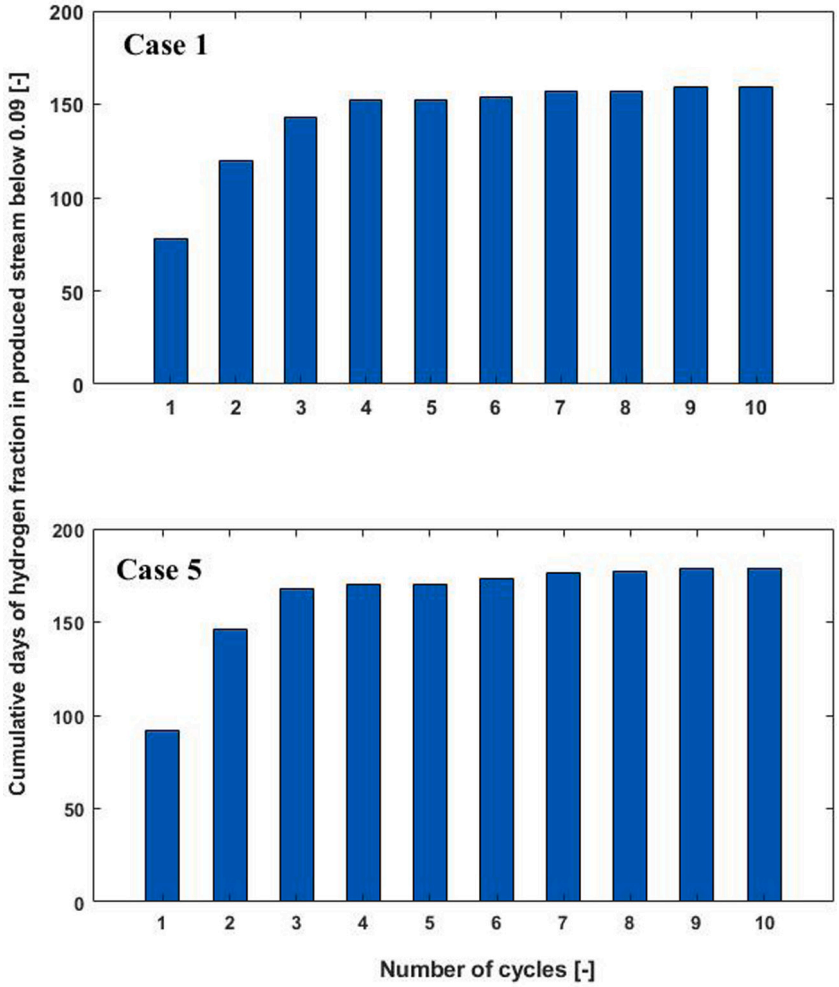

Fig. 7. Cumulative days in which the hydrogen fraction in the produced stream was less than 0.09 mol% of top: case 1; bottom: case 5.

shows the hydrogen fraction and gas saturation of the P50 realization in case 2. While the overall geometry is still circular for both hydrogen fraction and gas saturation (especially from the 5th cycle onwards), areas of high hydrogen fraction and gas saturation have irregular shapes (for reference, we also plot the permeability and porosity map of the same P50 realization in the appendix, see Fig. 15). The high gas saturation plume geometry aligns with the high permeability flow path at the top of the reservoir around the production well. A high hydrogen fraction plume (narrow yellow feature) developed down-dip where gas saturation is low which is consistent with case 1 (see left column of Fig. 4 and Fig. 8). Moreover, the hydrogen fraction in case 2 also increases with the number of cycles such as in case 1. The low hydrogen fraction area by the end of the 10th cycle is scattered around the whole gas plume which is different from case 1 where it presents as a half semi-circle geometry, see Fig. 4.

The general hydrogen fraction and gas saturation distribution pattern (permeability dependent, increasing hydrogen fraction, and final low hydrogen area) during cyclic operation of P50 in case 3 are the same as that of case 2, shown as Fig. 9. The major difference is that the gas plumes in case 3 are more uniform and complete, compared to case 2 where the high hydrogen fraction and gas saturation areas are interbedded by a narrow methane breakthrough flow path, e.g. see Fig. 2. In contrast, such flow path in realizations of case 3 tends to concentrate in one specific large area of the gas plume (top row Fig. 9).

The hydrogen fraction and gas saturation distribution pattern during cyclic operations in cases 6 and 7 do not show a distinct difference to that of cases 2 and 3 except for the structure (for detailed distribution of P50 in cases 6 and 7, readers can refer to appendix Figs. 13 and 14). As such, it is surprising that the small channel dimension will cause a distinct hydrogen fraction in the produced stream profiles in type 1 and 2 structures, shown in Fig. 10. In Fig. 10, cases 2 and 3 show similar P50, P90, and P10 regarding cumulative days of hydrogen fraction below 0.09, meanwhile, case 6 shows less cumulative days below 0.09 for both P50 and the difference between P90 and P10 (the uncertainty span) compared to case 7 (27% smaller for P50 and 31% smaller for the uncertainty span). Comparing case 2 with 6 (same channel body dimension in different structures), the P50 of the two cases is similar but the difference between P90 and P10 is not (case 6 shows 40% smaller uncertainty span). Interestingly, the situation is different when comparing case 3 with 7 (both large channel dimensions in different structures), their difference between P90 and P10 is nearly the same. However, case 7 shows 19% larger P50 than case 3. Finally, all four cases show increasing differences between P10 and P90 with the number of cycles (the length of the error bar is the shortest for 1st cycle of each case and longer for the consecutive cycles).

The big difference in cumulative days of hydrogen fraction in the produced stream below 0.09 in each case is the result of the combined effect of channel dimension and geological structure. Fig. 11 shows the variance of log permeability (x-axis) and dimensionless correlation length (y-axis) of first, middle, and last 10 percentile realizations in terms of cumulative days below 0.09 of each case (case 2 and 3 of type 1 structure, case 6 and 7 of type 2 structure). The dimensionless correlation length refers to the ratio between the range of variogram in major direction and the system length, which is an important index for

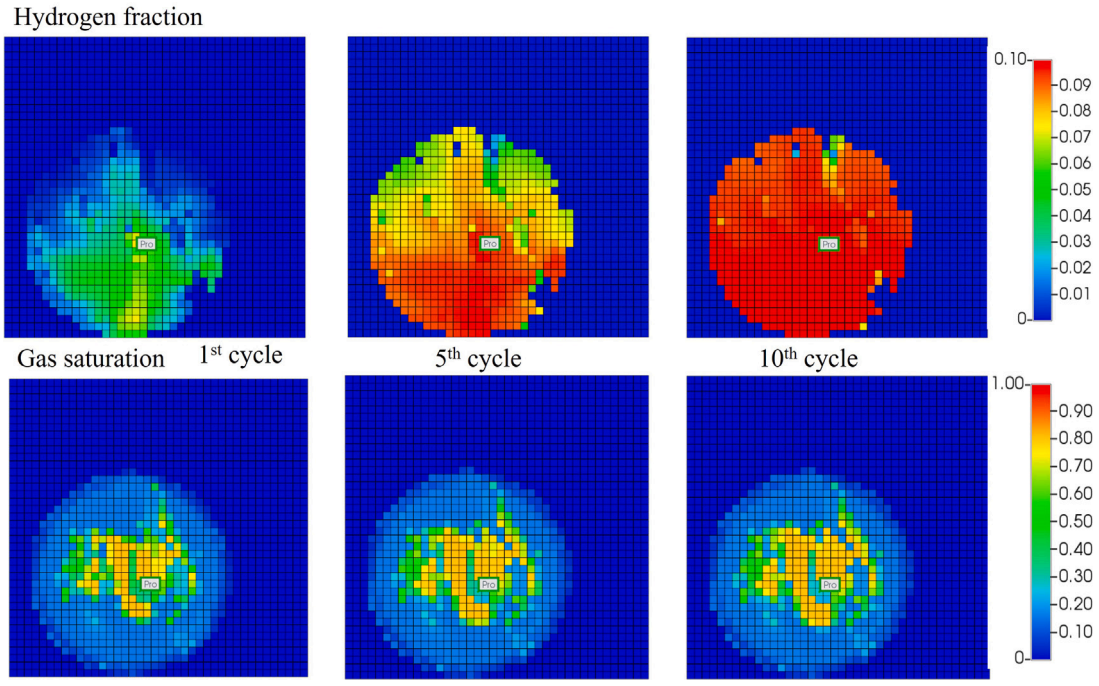

Fig. 8. Case 2 (heterogeneous, small channel) P50 result in map (areal) view on the top layer of the reservoir. Top row: hydrogen fraction distribution map; Bottom row: gas saturation distribution map; left: 1st cycle; middle: 5th cycle; right: 10th cycle.

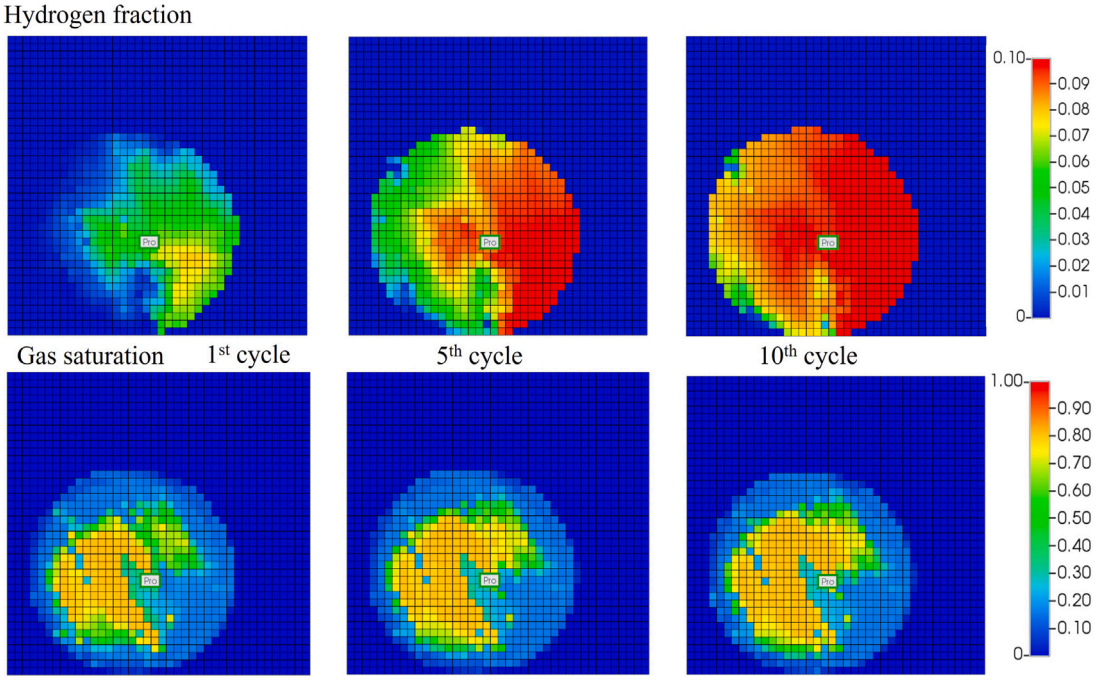

Fig. 9. Case 3 (heterogeneous, large channel) in map view. Top row: hydrogen fraction distribution map; Bottom row: gas saturation distribution map; left: 1st cycle; middle: 5th cycle; right: 10th cycle.

characterizing heterogeneity [94]. Through comparison, it is clear that, for the type 1 structure, changing the channel bodies dimension will not affect the heterogeneity considerably (left graph of Fig. 11). In contrast, a large channel will effectively increase the possibility of dimensionless correlation of the system in the type 2 structure to be above 1 (in type 1 structure, the possibility of this is comparable for large and small channel dimensions, see Fig. 11). Larger correlation length means longer flow paths and larger bypassed areas (Fig. 2), thus more severe

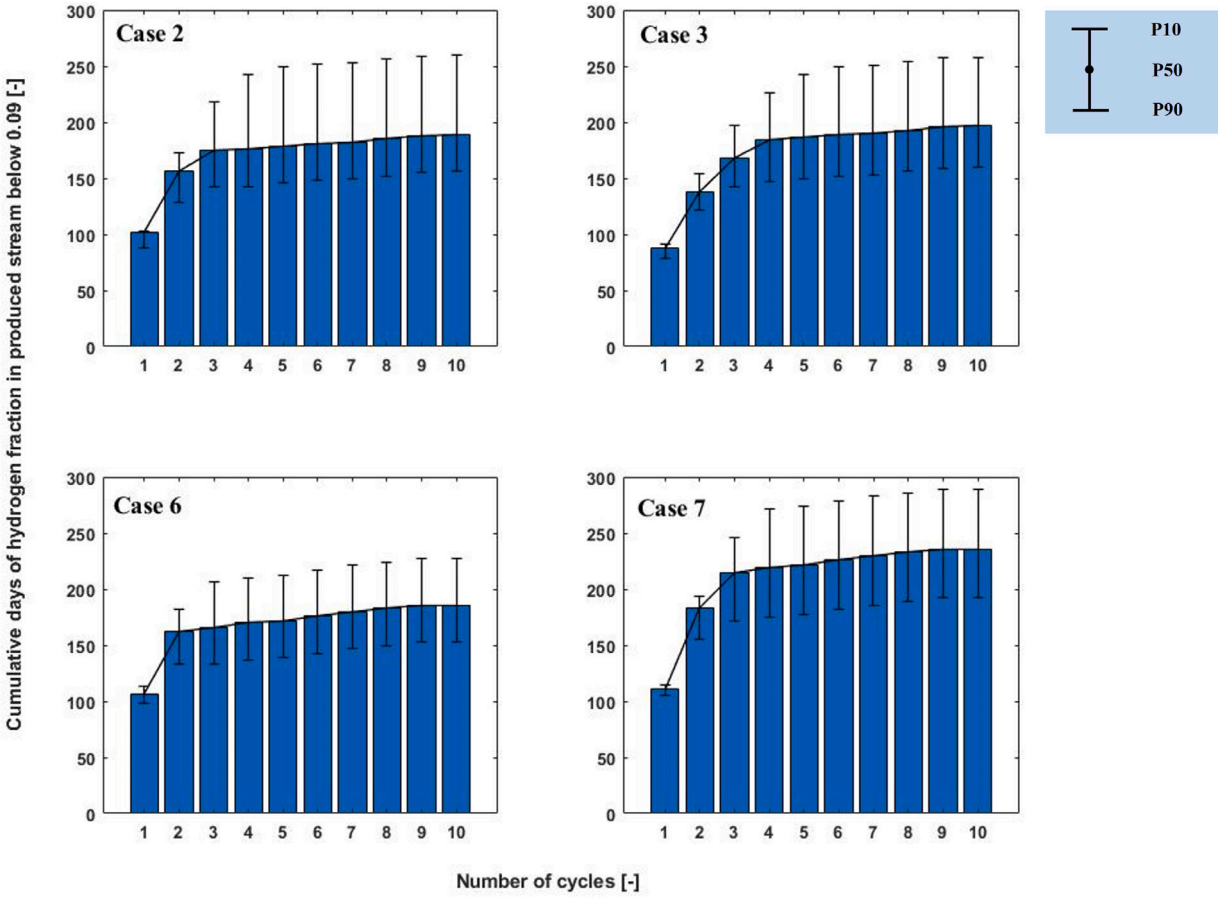

Fig. 10. Cumulative days the hydrogen fraction in the produced stream was less than 0.09 mol%. Top row: case 2 (left) and case 3 (right); bottom row: case 6 (left) and case 7(right); value of bars represents the P50 of each case; error bars represent the P90 and P10 of each case.

gas mixing during the production periods [94]. In contrast, smaller correlation lengths and variances of log permeability deliver miscible displacement with shorter flow paths (closer to uniform distribution) and smaller bypassed areas. This can be seen from Figs. 8 and 13 where lower hydrogen fraction areas are scattered and not as big as those in Fig. 9 and 14. Consequently, longer flow paths originated from facies distribution plus easier methane breakthrough in a type 2 structure (compared to type 1 structure) in case 7 bring about more severe gas mixing (more cumulative days and a bigger difference between P10 and P90 realizations compared to case 6, see bottom row of Fig. 10) affecting up to 15.8% of recovery. Facies heterogeneity is not as dominant as in type 1 structure due to its large closure area, the resulting log permeability variance and dimensionless correlation from small and large channel dimensions cannot be easily changed by the dimension of facies. As a result, the hydrogen fraction profiles of cases 2 and 3 are also comparable (top row of Fig. 10). It is noteworthy that the statistical model used for populating facies in cases 2 and 6, 3 and 7 are the same. Therefore, as discussed in the homogeneous cases section, the geological structures provide basic flow paths for potential gas fluids displacement, and the facies distributions determine the final flow path on which fluid displacement is going to happen (similar to the gravity dominant displacement described in [95]). The gas mixing will then depends on the dimension of such flow paths (dimensionless correlation and permeability variance).

3.3. Effects of injection/production rate

A large injection/production rate makes pure methane easier to breakthrough during production periods, leading to longer periods of the hydrogen fraction dropping below 0.09. Cases 4 and 8 double the injection/production rate and half the injection/production periods to test the effects of different rates while keeping the total injection/production volume the same as in the other cases. Fig. 12 shows the hydrogen fraction in the produced stream during production periods of cases 1, 4, 5, and 8. In the type 1 structure (left graph in Fig. 12), a certain amount of pure methane still resides at the bottom of the gas cap after 10 cycles which will breakthrough during production periods (see Fig. 4). Increasing the injection/production rate while keeping the total cycled volume of gas the same, will intensify the instability of the miscible displacement between the injected hydrogen-methane mixture (with lower viscosity) and the connate pure methane [96]. The higher the injection/production rate (the more viscous dominant the displacement), the further the hydrogen-methane mixture fingers will penetrate into the pure methane plume [45,97], leading to more severe gas mixing and easier pure methane breakthrough. From this perspective, the impact of higher injection/production rate will be more apparent with increasing hydrogen fraction in the stored stream (e.g. a pure hydrogen storage scenario) where the displacement is more unstable (greater mobility ratio) [97]. It is noteworthy that such effects of injection/production rate on gas mixing may vary in different systems. For example, the mixing zone geometry will be determined by formation structure when the displacement is gravity dominant, and by facies heterogeneity when the reservoir is highly heterogeneous [95, 96]. The injection/production rates effect on gas mixing observed here is then evident in relatively homogeneous reservoirs or reservoirs with a small correlation length [45].

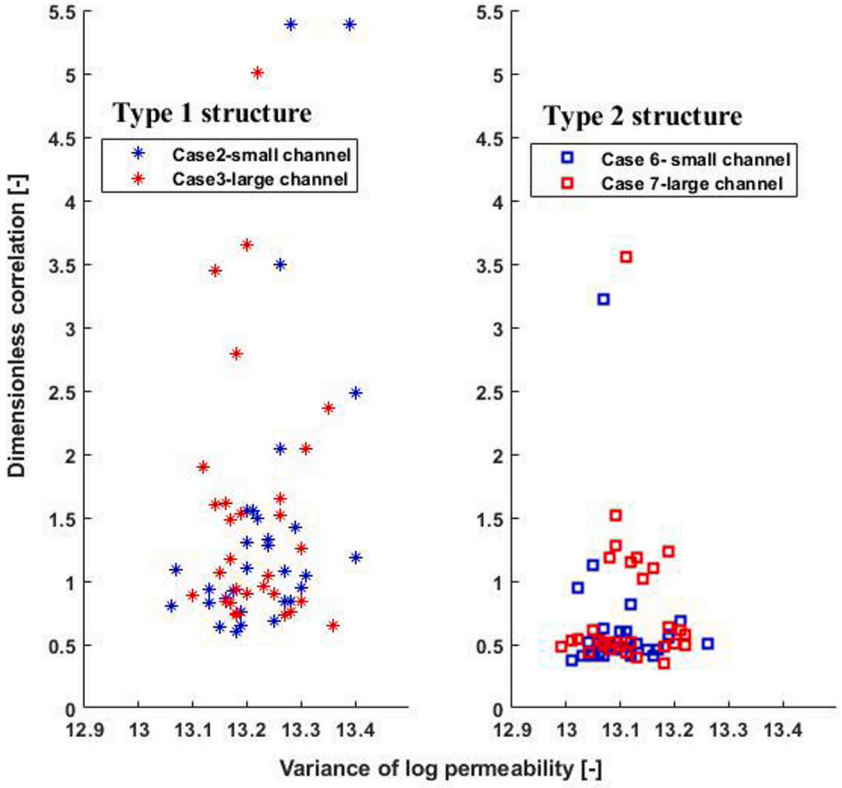

Fig. 11. Scatter plot of the variance of log permeability (x-axis) and dimensionless correlation (y-axis) of first, middle and last 10 percentile realizations. Left: type 1 structure (case 2 and 3); Right: type 2 structure (case 6 and 7).

Here, in cases 1 and 4, reservoirs are homogeneous. As a result, the cumulative days of hydrogen fraction below 0.09 of case 4 is 91 which is more than half of that for case 1 (159 days). The production periods of case 4 are half those of case 1, thus the cumulative days of hydrogen fraction below 0.09 are expected to be half of that if the gas mixing level in the two cases is the same. As a result, shown in Fig. 12, the hydrogen fraction in case 4 during the 10th cycle is always smaller than that of case 1. In contrast, in the type 2 structure, the connate pure methane is almost completely produced in case 5 after 10 cyclic operations (Fig. 5). Plus the easier methane breakthrough brought by increased rates (cumulative days of hydrogen fraction below 0.09 is 96, greater than half of 179 in case 5), a higher hydrogen fraction is achieved (not enough residual methane to get involved in gas mixing), shown as the right diagram of Fig. 12.

4. Conclusion

This study builds synthetic reservoirs in braided-fluvial system settings to investigate the effects of multi-level heterogeneity on gas mixing during UHS operations via reservoir-scale simulations. The petrophysical properties and sufficient aquifer support with open boundaries maintain the reservoir pressure and injectivity/productivity during the simulation. This allows the research to focus on the gas mixing processes. A 10 mol% hydrogen-methane mixture is used as stored fluids, following the UHS pilot project practices and avoiding major numerical errors around relative permeability (of hydrogen-methane mixture). Changing the hydrogen fraction (e.g. pure hydrogen storage) in stored fluids will result in a simultaneous increase in both mobility ratio and density difference. It is then expected that such a change will not affect the dominance of geological heterogeneity in hydrogen-methane miscible displacement under the same setting. Consequently, the following conclusions should also be applicable to pure hydrogen storage scenarios.

1. In homogeneous geological settings, steeper dip and closed boundaries will improve the vertical displacement of hydrogen, leading to an easier breakthrough of connate methane gas and up to 9.8% of recovery is affected. In such a situation, the hydrogen fraction in the produced stream will be lower than an open dome structure in the early cyclic period of a UHS project. However, due to the difficulty of producing the residing methane gas at the bottom of the gas cap from an open dome structure with a gentle dip, UHS in such a reservoir structure will struggle to reach a consistent hydrogen fraction similar to that of the injected fluids.

2. The heterogeneity of the depositional facies in a braided-fluvial setting will generally reduce the hydrogen fraction in the produced stream, affecting 15.8% of recovery in settings similar to our models (P90). The flow paths created by highly permeable channel bodies will concentrate the hydrogen displacement, degrading the sweep of hydrogen-rich fluids. Consequently, by-passed connate methane gas will reside in the reservoir and reduce the hydrogen fraction in the produced stream in the long term.

3. The geological structure is the first-order determining factor for the resulting heterogeneity indexes and flow regimes of a system. Facies heterogeneity may cause different flow patterns and subsequent hydrogen fraction profiles. From the results of this study, smaller channel dimensions in a steeply dipping formation may lead to a less flow path-dependent dispersive flow regime that delivers higher hydrogen fraction profiles and less uncertainty. In contrast, a gentler reservoir formation dip implies a larger closure area and similar heterogeneity indexes from different channel dimensions. The subsequent flow pattern and hydrogen fraction profiles will also be comparable.

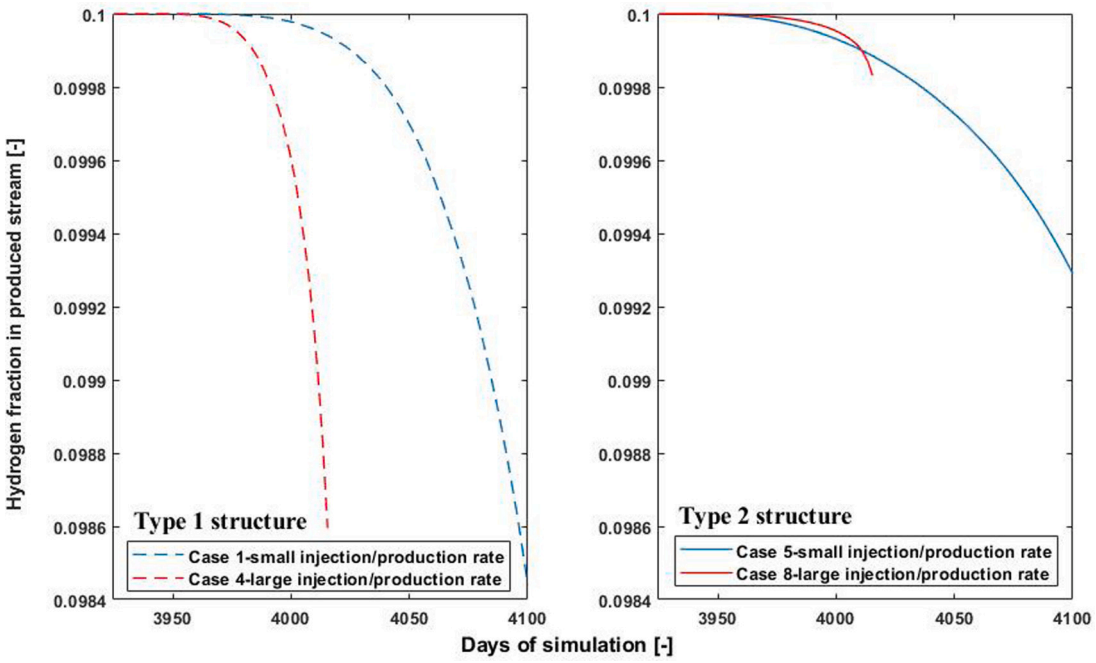

Fig. 12. Hydrogen fraction profiles during 10th cycle. Left: case 1 (blue dash line) and 4 (red dash line); Right: case 5 (blue line) and 8 (red line). (For interpretation of the references to color in this figure legend, the reader is referred to the web version of this article.)

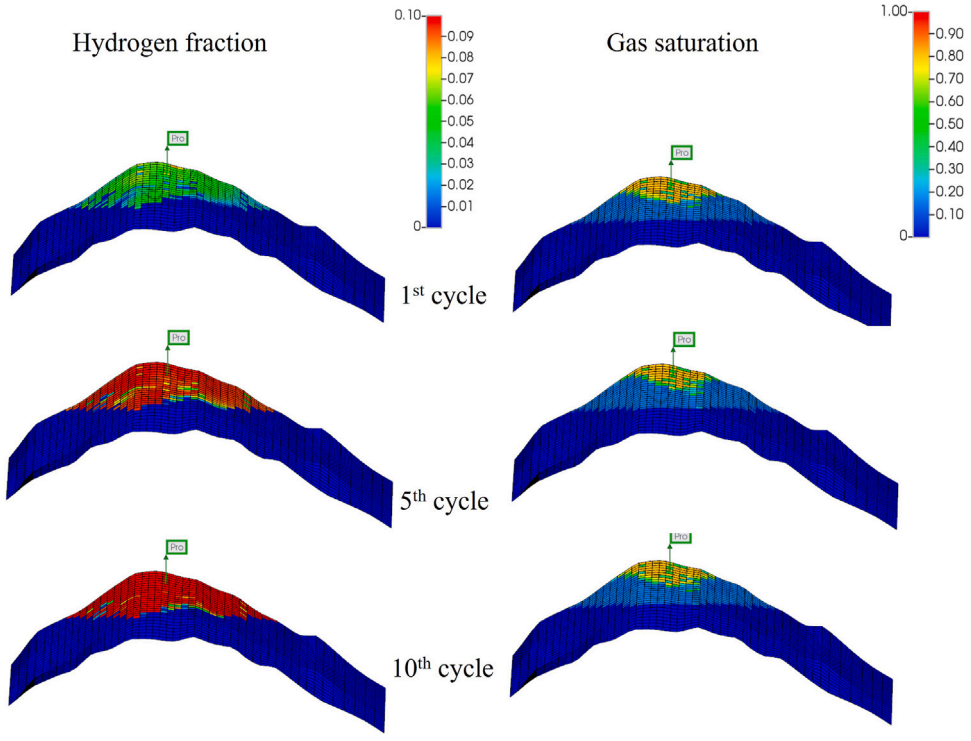

Fig. 13. Case 6 Left column: hydrogen fraction distribution map; Right column: gas saturation distribution map; at the end of top: 1st cycle; middle: 5th cycle; bottom: 10th cycle.

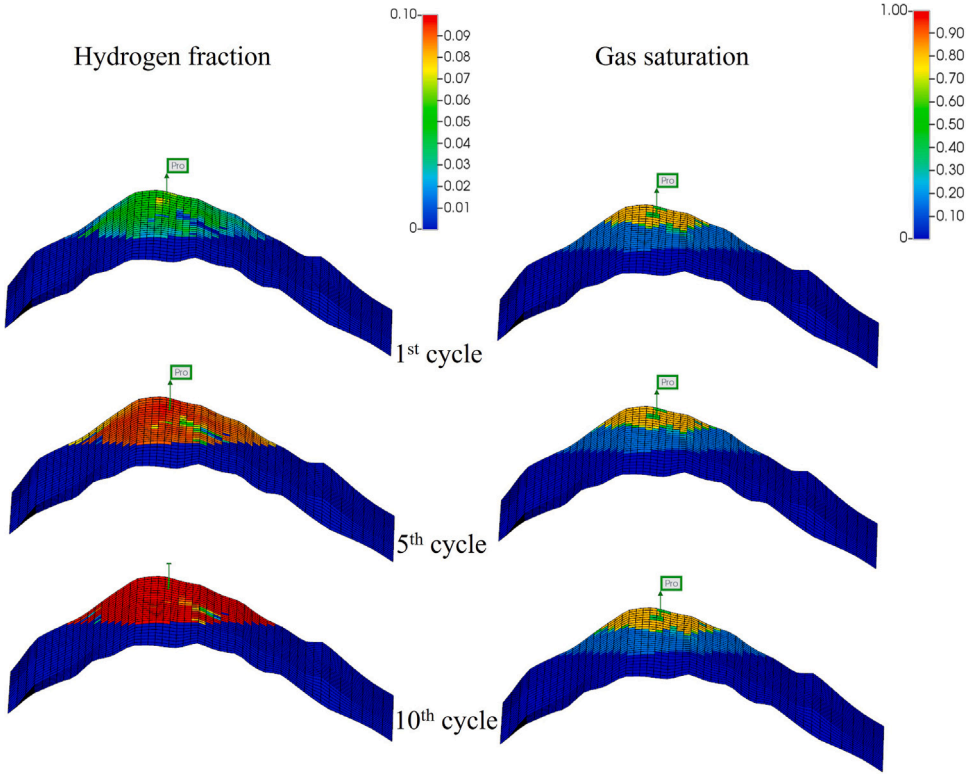

Fig. 14. Case 7 Left column: hydrogen fraction distribution map; Right column: gas saturation distribution map; at the end of top: 1st cycle; middle: 5th cycle; bottom: 10th cycle.

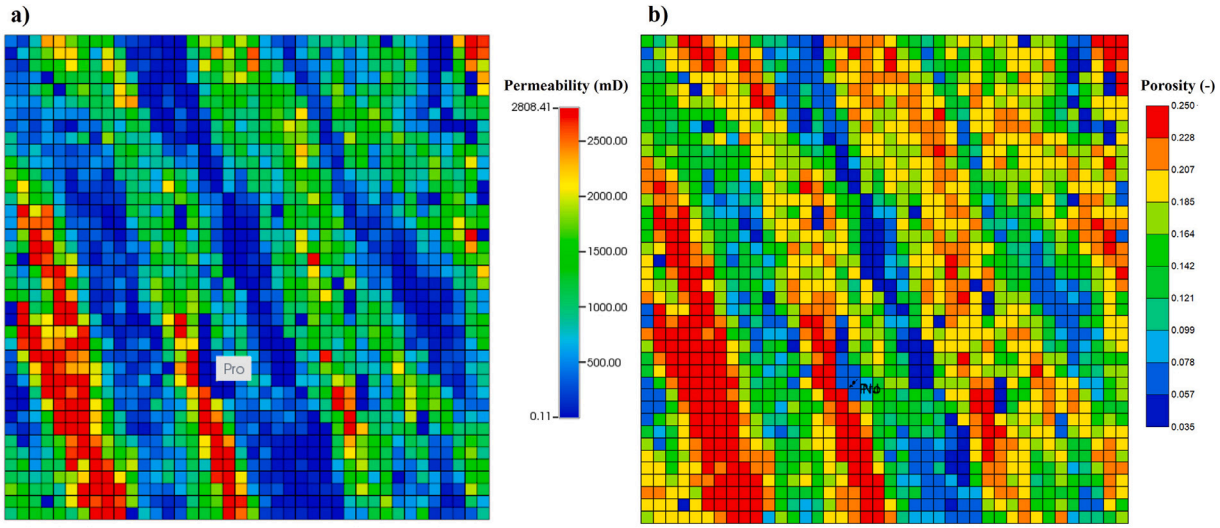

Fig. 15. (a) Areal view of permeability of top layer of case 2 P50 realization; (b) Areal view of porosity of top layer of case 2 P50 realization.

4. Increasing the injection/production rate may improve the ultimate hydrogen fraction profiles by helping the breakthrough of connate gas in the reservoir. However, geological structure is still the determining factor of this process, hydrogen fraction will be lower when increasing the injection/production rate in some reservoirs with small formation dips where vertical displacement of connate methane is relatively poor.

The results of this simulation study indicate that careful consideration of the depositional environment and its implications in flow

property distribution of potential storage reservoirs needs to be given for the design of UHS projects.

CRediT authorship contribution statement

Zhenkai Bo: Writing – original draft, Visualization, Software, Methodology, Investigation, Formal analysis. **Sebastian Hörning:** Writing – review & editing, Supervision, Software, Methodology. **Jim R. Underschultz:** Writing – review & editing, Supervision, Conceptualization. **Andrew Garnett:** Writing – review & editing, Funding acquisition, Conceptualization. **Suzanne Hurter:** Writing – review & editing, Visualization, Methodology, Funding acquisition, Conceptualization.

Declaration of competing interest

The authors declare that they have no known competing financial interests or personal relationships that could have appeared to influence the work reported in this paper.

Data availability

Data will be made available on request.

Acknowledgments

This research has been partially funded by the Energi Simulation Industrial Chair program. Energi Simulation is a not-for-profit organization based in Canada. This research has also been funded by The University of Queensland Centre for Natural Gas (CNG) and its industry members (Arrow Energy, Australia Pacific LNG and Santos). Zhenkai acknowledges the University of Queensland and Energi Simulation for the University of Queensland Research Training Stipend and Research Higher Degree Top Up Scholarships.

Appendix A. Complementary figures of heterogeneous cases

See Figs. 13–15.

Appendix B. Sensitivity of dispersivity and numerical dispersion

Dispersion of fluid happens when several different fluids mix in the medium due to molecular diffusion at a relatively low velocity and mechanical advection at a relatively high velocity [48]. Parameter dispersivity is commonly used in numerical simulation for characterizing the dispersion length scale which is not considered in the present numerical simulation study. To understand the potential impact of dispersion on the UHS simulation at the reservoir-scale, we performed sensitivity analysis on the resulting cumulative hydrogen production with various dispersivities in UHS simulation using our homogeneous models (case 5). To date, there is only one experimental study that reports the dispersivity of hydrogen in nitrogen gas (0.0003077 m) in a Berea Sandstone core sample [98]. In order to get the potential upper and lower limits of impacts from dispersion, the author uses the variation in carbon dioxide dispersivity in methane across a range of superficial velocities, spanning from 0.14 to 0.628 mm/s, which corresponds to a range of 40% to 440% of the mean dispersivity [99]. By extrapolating this variation range to hydrogen, dispersivity values ranging from 0.00012308 to 0.00125388 m are derived. These dispersivity values are introduced into simulation cases to assess the impact of dispersion over a 30-year reservoir-scale simulation (the other simulation setup remains the same as in this study). Fig. 16 shows the resulting absolute mass difference of cumulative hydrogen production over the 30-year simulation time between simulation cases considering median (black curve), high (red curve), and low dispersivity (blue curve) and a simulation case without modeling dispersion via dispersivity (dispersivity equals 0). It is clear that the largest difference does not exceed 35 kg which is smaller than 0.001% of the result. Note that the highest absolute mass difference comes from the simulation case with median dispersivity and the resulting differences between simulation cases using high and low dispersivity are comparable. This means applying lower or higher dispersivity than those used here is unlikely to increase the simulation error.

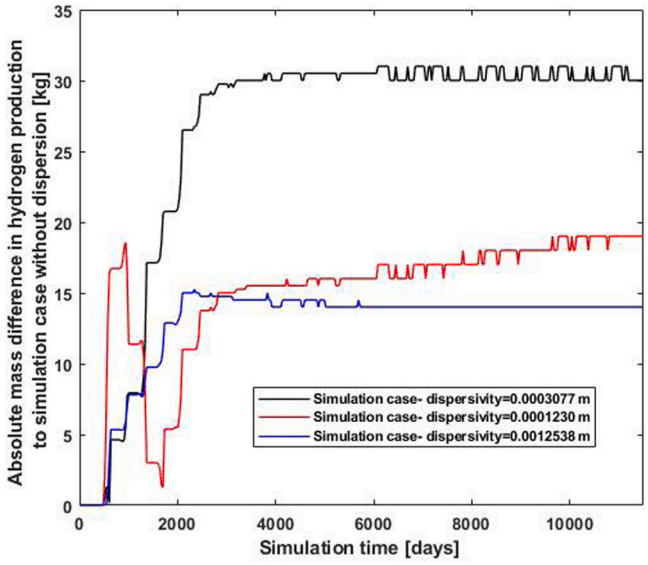

Fig. 16. Absolute mass differences of cumulative hydrogen production over simulation time between simulation cases with black curve: median dispersivity; red curve: high dispersivity; blue curve: low dispersivity; and simulation case without considering dispersion. (For interpretation of the references to color in this figure legend, the reader is referred to the web version of this article.)

Maniglio et al. [92] investigate the numerical dispersion during UHS reservoir-scale numerical simulation. They find that, for a coarse grid size (e.g. grid size in this study), the numerical dispersion and heterogeneity-induced dispersion are comparable. Therefore, by comparing the hydrogen fraction in the produced stream (as presented in this study), the effects of heterogeneity on gas mixing can be evaluated [92]. Moreover, inherently the advection–dispersion equation, as long as it is not solved at pore-scale, cannot distinguish between mixing (dispersion) and spreading. The resulting breakthrough curve is acceptable [57] (given the reaction is not simulated in this study). In other words, we believe the comparative method in this study is sufficient for quantifying the effects of different levels of heterogeneity on gas mixing in terms of the numerical simulation brought by the grid size.

Finally, to justify the discretization of our geological model, grid sizes from $10 * 10$ m to $40 * 40$ m are tested for the same injection and production scheme. We found that the grid size of $10 * 10$ m is computationally infeasible for performing reservoir-scale simulation of UHS because tens of days will be needed to finish a single simulation. Moreover, simulation using a grid size $20 * 20$ m enlarges the required computation time from around 30 min to nearly one day with no significant difference in results compared to a grid size of $40 * 40$ m. Therefore, we decided to use the grid size of $40 * 40$ m in our simulation study. Detailed results of these test simulations regarding grid sizes can be found in our previous study [88].

Appendix C. Average reservoir pressure and cumulative hydrogen and methane production

See Fig. 17.

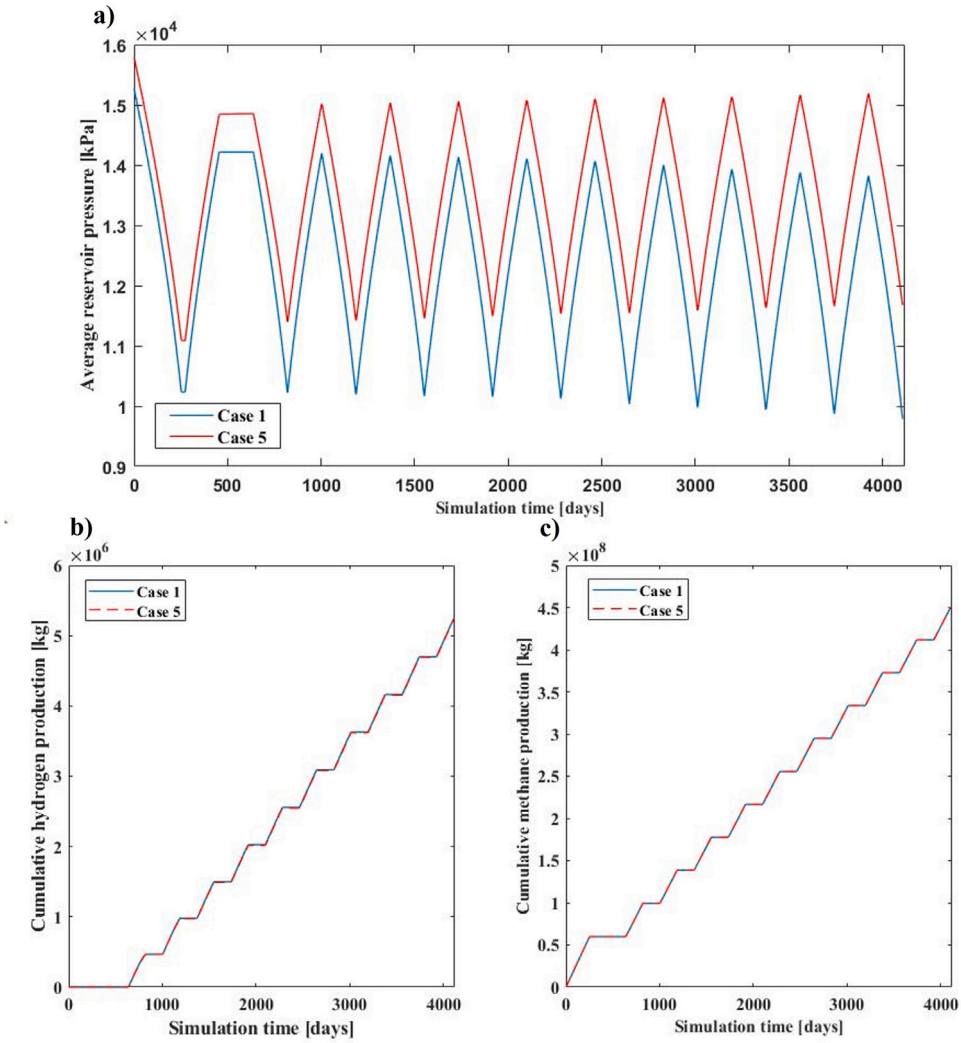

Fig. 17. (a) The average reservoir pressure history during the simulation; (b) The cumulative hydrogen production of cases 1 and 5, the difference is less than 0.2%; (c) The cumulative methane production of cases 1 and 5, difference is less than 0.02%.

References

[1] Hanley ES, Deane J, Gallachoir BO. The role of hydrogen in low carbon energy futures–a review of existing perspectives. Renew Sustain Energy Rev 2018;82:3027–45. http://dx.doi.org/10.1016/j.rser.2017.10.034, URL https://www.sciencedirect.com/science/article/pii/S1364032117314089.

[2] Kovač A, Paranos M, Marciuš D. Hydrogen in energy transition: A review. Int J Hydrogen Energy 2021;46(16):10016–35. http://dx.doi.org/10.1016/j.ijhydene.2020.11.256, URL https://www.sciencedirect.com/science/article/pii/S0360319920345079.

[3] Li X, Raorane CJ, Xia C, Wu Y, Tran TKN, Khademi T. Latest approaches on green hydrogen as a potential source of renewable energy towards sustainable energy: Spotlighting of recent innovations, challenges, and future insights. Fuel 2023;334:126684. http://dx.doi.org/10.1016/j.fuel.2022.126684, URL https://www.sciencedirect.com/science/article/pii/S0016236122035086.

[4] Miao B, Giordano L, Chan SH. Long-distance renewable hydrogen transmission via cables and pipelines. Int J Hydrogen Energy 2021;46(36):18699–718. http://dx.doi.org/10.1016/j.ijhydene.2021.03.067, URL https://www.sciencedirect.com/science/article/pii/S0360319921009137.

[5] van Renssen S. The hydrogen solution? Nature Clim Change 2020;10(9):799–801. http://dx.doi.org/10.1038/s41558-020-0891-0, Number: 9 Publisher: Nature Publishing Group URL https://www.nature.com/articles/s41558-020-0891-0.

[6] Abad AV, Dodds PE. Green hydrogen characterisation initiatives: Definitions, standards, guarantees of origin, and challenges. Energy Policy 2020;138:111300.

[7] Howarth RW, Jacobson MZ. How green is blue hydrogen? Energy Sci Eng 2021;9(10):1676–87.

[8] IEA. Global hydrogen review. Tech. rep., Paris: IEA; 2022, p. 72.

[9] Mouli-Castillo J, Heinemann N, Edlmann K. Mapping geological hydrogen storage capacity and regional heating demands: An applied UK case study. Appl Energy 2020;116348, Publisher: Elsevier.

[10] Perera MSA. A review of underground hydrogen storage in depleted gas reservoirs: Insights into various rock-fluid interaction mechanisms and their impact on the process integrity. Fuel 2023;334:126677. http://dx.doi.org/10.1016/j.fuel.2022.126677, URL https://www.sciencedirect.com/science/article/pii/S0016236122035013.

[11] Noussan M, Raimondi PP, Scita R, Hafner M. The role of green and blue hydrogen in the energy transition—A technological and geopolitical perspective. Sustainability 2020;13(1):298.

[12] Bruce S, Temminghoff M, Hayward J, Schmidt E, Munnings C, Palfreyman D, et al. National hydrogen roadmap. Tech. rep., CSIRO; 2018, p. 1–100.

[13] Hassanpouryouzband A, Joonaki E, Edlmann K, Haszeldine RS. Offshore geological storage of hydrogen: Is this our best option to achieve net-zero? ACS Energy Lett 2021;6(6):2181–6.

[14] Raza A, Arif M, Glatz G, Mahmoud M, Al Kobaisi M, Alafnan S, et al. A holistic overview of underground hydrogen storage: Influencing factors, current understanding, and outlook. Fuel 2022;330:125636.

[15] Wallace RL, Cai Z, Zhang H, Zhang K, Guo C. Utility-scale subsurface hydrogen storage: UK perspectives and technology. Int J Hydrogen Energy 2021;46(49):25137–59.

[16] Gregory DP. The hydrogen economy. Sci Am 1973;228(1):13–21, URL http://www.jstor.org/stable/24922952.

[17] Tarkowski R. Underground hydrogen storage: Characteristics and prospects. Renew Sustain Energy Rev 2019;105:86–94.

[18] Bai M, Song K, Sun Y, He M, Li Y, Sun J. An overview of hydrogen underground storage technology and prospects in China. J Pet Sci Eng 2014;124:132–6.

[19] Tarkowski R, Uliasz-Misiak B. Towards underground hydrogen storage: A review of barriers. Renew Sustain Energy Rev 2022;162:112451.

[20] Carden P, Paterson L. Physical, chemical and energy aspects of underground hydrogen storage. Int J Hydrogen Energy 1979;4(6):559–69.

[21] Pan B, Yin X, Ju Y, Iglauer S. Underground hydrogen storage: Influencing parameters and future outlook. Adv Colloid Interface Sci 2021;294:102473.

[22] Labus K, Tarkowski R. Modeling hydrogen – rock – brine interactions for the Jurassic reservoir and cap rocks from Polish Lowlands. Int J Hydrogen Energy 2022;47(20):10947–62. http://dx.doi.org/10.1016/j.ijhydene.2022.01.134, URL https://www.sciencedirect.com/science/article/pii/S0360319922002518.

[23] Schulz P. The effects of hydrogen injection in natural gas networks for the Dutch underground storages. Tech. rep., Netherlands Enterprise Agency; 2017, p. 1–100.

[24] Ugarte ER, Salehi S. A review on well integrity issues for underground hydrogen storage. J Energy Res Technol 2022;144(4).

[25] Bo Z, Zeng L, Chen Y, Xie Q. Geochemical reactions-induced hydrogen loss during underground hydrogen storage in sandstone reservoirs. Int J Hydrogen Energy 2021;46(38):19998–20009.

[26] Dopffel N, Jansen S, Gerritse J. Microbial side effects of underground hydrogen storage–Knowledge gaps, risks and opportunities for successful implementation. Int J Hydrogen Energy 2021;46(12):8594–606, Publisher: Elsevier.

[27] Thaysen EM, McMahon S, Strobel GJ, Butler IB, Ngwenya BT, Heinemann N, et al. Estimating microbial growth and hydrogen consumption in hydrogen storage in porous media. Renew Sustain Energy Rev 2021;151:111481.

[28] Ennis-King J, Michael K, Strand J, Sander R, Green C. Underground storage of hydrogen: mapping out options for Australia. Future Fuel CRC; 2021.

[29] Gasanzade F, Pfeiffer WT, Witte F, Tuschy I, Bauer S. Subsurface renewable energy storage capacity for hydrogen, methane and compressed air–a performance assessment study from the North German Basin. Renew Sustain Energy Rev 2021;149:111422, Publisher: Elsevier.

[30] Al-Mukainah H, Al-Yaseri A, Yekeen N, Al Hamad J, Mahmoud M. Wettability of shale–brine–H2 system and H2-brine interfacial tension for assessment of the sealing capacities of shale formations during underground hydrogen storage. Energy Rep 2022;8:8830–43.

[31] Iglauer S, Ali M, Keshavarz A. Hydrogen wettability of sandstone reservoirs: Implications for hydrogen geo-storage. Geophys Res Lett 2021;48(3). e2020GL090814.

[32] Pan B, Liu K, Ren B, Zhang M, Ju Y, Gu J, et al. Impacts of relative permeability hysteresis, wettability, and injection/withdrawal schemes on underground hydrogen storage in saline aquifers. Fuel 2023;333:126516. http://dx.doi.org/10.1016/j.fuel.2022.126516, URL https://www.sciencedirect.com/science/article/pii/S0016236122033403.

[33] Luboń K, Tarkowski R. Numerical simulation of hydrogen injection and withdrawal to and from a deep aquifer in NW Poland. Int J Hydrogen Energy 2020;45(3):2068–83.

[34] Lysyy M, Fernø M, Ersland G. Seasonal hydrogen storage in a depleted oil and gas field. Int J Hydrogen Energy 2021;46(49):25160–74. http://dx.doi.org/10.1016/j.ijhydene.2021.05.030, URL https://www.sciencedirect.com/science/article/pii/S0360319921017444.

[35] Hassanpouryouzband A, Adie K, Cowen T, Thaysen EM, Heinemann N, Butler IB, et al. Geological hydrogen storage: Geochemical reactivity of hydrogen with sandstone reservoirs. ACS Energy Lett 2022;7:2203–10.

[36] Veshareh MJ, Thaysen EM, Nick HM. Feasibility of hydrogen storage in depleted hydrocarbon chalk reservoirs: Assessment of biochemical and chemical effects. Appl Energy 2022;323:119575, Publisher: Elsevier.

[37] Liu N, Kovscek AR, Fernø MA, Dopffel N. Pore-scale study of microbial hydrogen consumption and wettability alteration during underground hydrogen storage. Front Energy Res 2023;11:1124621.

[38] Boon M, Hajibeygi H. Experimental characterization of H_2/water multiphase flow in heterogeneous sandstone rock at the core scale relevant for underground hydrogen storage (UHS). Sci Rep 2022;12.

[39] Jangda Z, Menke H, Busch A, Geiger S, Bultreys T, Lewis H, et al. Pore-scale visualization of hydrogen storage in a sandstone at subsurface pressure and temperature conditions: Trapping, dissolution and wettability. J Colloid Interface Sci 2023;629:316–25. http://dx.doi.org/10.1016/j.jcis.2022.09.082, URL https://www.sciencedirect.com/science/article/pii/S0021979722016678.

[40] Yu M, Wang K, Vredenburg H. Insights into low-carbon hydrogen production methods: Green, blue and aqua hydrogen. Int J Hydrogen Energy 2021;46(41):21261–73.

[41] Ismael M. Latest progress on the key operating parameters affecting the photocatalytic activity of TiO2-based photocatalysts for hydrogen fuel production: A comprehensive review. Fuel 2021;303:121207. http://dx.doi.org/10.1016/j.fuel.2021.121207, URL https://www.sciencedirect.com/science/article/pii/S0016236121010863.

[42] Batterham R, Domansky K, Brear M, Smart S, Greig C, Bolt R. Net zero mobilisation report: How to make net zero happen | net zero Australia. Tech. rep., Online: Net Zero Australia; 2023, p. 26–7.

[43] Reitenbach V, Ganzer L, Albrecht D, Hagemann B. Influence of added hydrogen on underground gas storage: A review of key issues. Environ Earth Sci 2015;73(11):6927–37.

[44] Zamehrian M, Sedaee B. Underground hydrogen storage in a partially depleted gas condensate reservoir: Influence of cushion gas. J Pet Sci Eng 2022;212:110304, Publisher: Elsevier.

[45] Wang G, Pickup G, Sorbie K, Mackay E. Scaling analysis of hydrogen flow with carbon dioxide cushion gas in subsurface heterogeneous porous media. Int J Hydrogen Energy 2022;47(3):1752–64.

[46] Dawood F, Anda M, Shafiullah GM. Hydrogen production for energy: An overview. Int J Hydrogen Energy 2020;45(7):3847–69. http://dx.doi.org/10.1016/j.ijhydene.2019.12.059, URL https://www.sciencedirect.com/science/article/pii/S0360319919345926.

[47] Ershadnia R, Singh M, Mahmoodpour S, Meyal A, Moeini F, Hosseini SA, et al. Impact of geological and operational conditions on underground hydrogen storage. Int J Hydrogen Energy 2022.

[48] Feldmann F, Hagemann B, Ganzer L, Panfilov M. Numerical simulation of hydrodynamic and gas mixing processes in underground hydrogen storages. Environ Earth Sci 2016;75(16):1165, Publisher: Springer.

[49] Kanaani M, Sedaee B, Asadian-Pakfar M. Role of cushion gas on underground hydrogen storage in depleted oil reservoirs. J Energy Storage 2022;45:103783.

[50] Pfeiffer WT, Bauer S. Subsurface porous media hydrogen storage–scenario development and simulation. Energy Procedia 2015;76:565–72.

[51] Hashemi L, Boon M, Glerum W, Farajzadeh R, Hajibeygi H. A comparative study for H2–CH4 mixture wettability in sandstone porous rocks relevant to underground hydrogen storage. Adv Water Resour 2022;163:104165.

[52] Graham GH, Jackson MD, Hampson GJ. Three-dimensional modeling of clinoforms in shallow-marine reservoirs: Part 2. Impact on fluid flow and hydrocarbon recovery in fluvial-dominated deltaic reservoirs. AAPG Bull 2015;99(6):1049–80.

[53] Jordan DW, Pryor WA. Hierarchical levels of heterogeneity in a Mississippi River meander belt and application to reservoir systems. AAPG Bull 1992;76(10):1601–24, Publisher: American Association of Petroleum Geologists (AAPG).

[54] Jones A, Doyle J, Jacobsen T, Kjønsvik D. Which sub-seismic heterogeneities influence waterflood performance? A case study of a low net-to-gross fluvial reservoir. Geol Soc Lond Special Publ 1995;84(1):5–18, Publisher: Geological Society of London.

[55] Menke HP, Maes J, Geiger S. Channeling is a distinct class of dissolution in complex porous media. Sci Rep 2023;13(1):11312.

[56] Wang YD, Meyer Q, Tang K, McClure JE, White RT, Kelly ST, et al. Large-scale physically accurate modelling of real proton exchange membrane fuel cell with deep learning. Nature Commun 2023;14(1):745.

[57] Carrera J, Saaltink MW, Soler-Sagarra J, Wang J, Valhondo C. Reactive transport: A review of basic concepts with emphasis on biochemical processes. Energies 2022;15(3):925.

[58] Ringrose P, Bentley M. Reservoir model design, Vol. 467. Springer; 2016.

[59] Li D, Lake LW. Scaling fluid flow through heterogeneous permeable media. SPE Adv Technol Ser 1995;3(01):188–97, Publisher: OnePetro.

[60] Chang Y-B, Lim M, Pope G, Sepehrnoori K. CO2 flow patterns under multiphase flow: Heterogeneous field-scale conditions. SPE Res Eng 1994;9(03):208–16.

[61] Okoroafor ER, Saltzer SD, Kovscek AR. Toward underground hydrogen storage in porous media: Reservoir engineering insights. Int J Hydrogen Energy 2022;47(79):33781–802.

[62] Heinemann N, Scafidi J, Pickup G, Thaysen E, Hassanpouryouzband A, Wilkinson M, et al. Hydrogen storage in saline aquifers: The role of cushion gas for injection and production. Int J Hydrogen Energy 2021;46(79):39284–96.

[63] Galloway WE, Hobday DK. Terrigenous clastic depositional systems: applications to petroleum, coal, and uranium exploration. Springer Science & Business Media; 2012.

[64] Doeglas D. The structure of sedimentary deposits of braided rivers. Sedimentology 1962;1(3):167–90.

[65] Miall AD. A review of the braided-river depositional environment. Earth-Sci Rev 1977;13(1):1–62.

[66] Miall AD. Architectural-element analysis: A new method of facies analysis applied to fluvial deposits. Earth-Sci Rev 1985;22(4):261–308. http://dx.doi.org/10.1016/0012-8252(85)90001-7, URL https://www.sciencedirect.com/science/article/pii/0012825285900017.

[67] Miall AD. The geology of fluvial deposits: sedimentary facies, basin analysis, and petroleum geology. Springer; 2013.

[68] Gibling MR. Width and thickness of fluvial channel bodies and valley fills in the geological record: A literature compilation and classification. J Sediment Res 2006;76(5):731–70, Publisher: SEPM Society for Sedimentary Geology.

[69] Potter PE. Sand bodies and sedimentary environments: A review. AAPG Bull 1967;51(3):337–65.

[70] Colombera L, Mountney NP, McCaffrey WD. A quantitative approach to fluvial facies models: Methods and example results. Sedimentology 2013;60(6):1526–58.

[71] Conway AM, Valvatne C. The Murdoch gas field, block 44/22a, UK Southern North Sea. Geol Soc Lond Memoirs 2003;20(1):789–98, Publisher: Geological Society of London.

[72] La Croix AD, He J, Bianchi V, Wang J, Gonzalez S, Undershultz JR. Early Jurassic palaeoenvironments in the Surat Basin, Australia–marine incursion into eastern Gondwana. Sedimentology 2020;67(1):457–85, Publisher: Wiley Online Library.

[73] Melvin J. Evolving fluvial style in the Kekiktuk formation (Mississippian), Endicott field area, Alaska: base level response to contemporaneous tectonism. AAPG Bull 1993;77(10):1723–44, Publisher: American Association of Petroleum Geologists (AAPG).

[74] Hovorka SD, Doughty C, Benson SM, Pruess K, Knox PR. The impact of geological heterogeneity on CO2 storage in brine formations: A case study from the Texas Gulf Coast. Geol Soc Lond Special Publ 2004;233(1):147–63.
[75] Atkinson CD, McGowen JH, Bloch S, Lundell LL, Trumbly PN. Braidplain and deltaic reservoir, Prudhoe Bay field, Alaska. In: Sandstone petroleum reservoirs. Springer; 1990, p. 7–29.
[76] Energy S. Dynamic modelling workflow for the underground gas storage project, onshore otway basin. Tech. rep. victorian gas program technical report 41, Geological Survey of Victoria. Department of Jobs; 2020.
[77] Mitra S, Leslie W. Three-dimensional structural model of the Rhourde el Baguel field, Algeria. AAPG Bull 2003;87(2):231–50.
[78] La Croix AD, Wang J, He J, Hannaford C, Bianchi V, Esterle J, et al. Widespread nearshore and shallow marine deposition within the lower Jurassic precipice sandstone and evergreen formation in the Surat basin, Australia. Mar Pet Geol 2019;109:760–90.
[79] Jr Sam Boggs. Principles of sedimentology and stratigraphy. 5th ed.. Boston: Pearson; 2011.
[80] Gershenzon NI, Ritzi RW, Dominic DF, Mehnert E, Okwen RT. Capillary trapping of CO2 in heterogeneous reservoirs during the injection period. Int J Greenhouse Gas Control 2017;59:13–23. http://dx.doi.org/10.1016/j.ijggc.2017.02.002, URL https://www.sciencedirect.com/science/article/pii/S1750583616306119.
[81] SLB. User's guide, petrel E&P software plateform (version 2019). SLB. SLB; 2020, URL https://www.software.slb.com/products/petrel/petrel-geology-and-modeling.
[82] Pyrcz MJ, Deutsch CV. Geostatistical reservoir modeling. Oxford University Press; 2014.
[83] Reinfelds I, Nanson G. Formation of braided river floodplains, Waimakariri river, new Zealand. Sedimentology 1993;40(6):1113–27.
[84] Energy S. A petrophysical model of the waarre formation in the port campbell embayment. Tech. rep. victorian gas program technical report 17, Geological Survey of Victoria; 2020.
[85] Alizadeh A, Piri M. Three-phase flow in porous media: A review of experimental studies on relative permeability. Rev Geophys 2014;52(3):468–521.
[86] Yekta AE, Manceau J-C, Gaboreau S, Pichavant M, Audigane P. Determination of hydrogen–water relative permeability and capillary pressure in sandstone: Application to underground hydrogen injection in sedimentary formations. Transp Porous Media 2018;122(2):333–56, Publisher: Springer.
[87] Lysyy M, Føyen T, Johannesen EB, Fernø M, Ersland G. Hydrogen relative permeability hysteresis in underground storage. Geophys Res Lett 2022;49(17). http://dx.doi.org/10.1029/2022GL100364, e2022GL100364, URL https://onlinelibrary.wiley.com/doi/abs/10.1029/2022GL100364.
[88] Bo Z, Boon M, Hajibeygi H, Hurter S. Impact of experimentally measured relative permeability hysteresis on reservoir-scale performance of underground hydrogen storage (UHS). Int J Hydrogen Energy 2023;48(36):13527–42. http://dx.doi.org/10.1016/j.ijhydene.2022.12.270.
[89] Ershadnia R, Hajirezaie S, Amooie A, Wallace CD, Gershenzon NI, Hosseini SA, et al. CO2 geological sequestration in multiscale heterogeneous aquifers: Effects of heterogeneity, connectivity, impurity, and hysteresis. Adv Water Resour 2021;151:103895.
[90] Aziz K. Petroleum reservoir simulation. Appl Sci Publ 1979;476.
[91] Wang Y, Vuik C, Hajibeygi H. Analysis of hydrodynamic trapping interactions during full-cycle injection and migration of CO2 in deep saline aquifers. Adv Water Resour 2022;159:104073.
[92] Maniglio M, Pizzolato A, Panfili P, Cominelli A. A simple and practical approach to estimate dispersive mixing in underground hydrogen storage systems. In: SPE annual technical conference and exhibition?. SPE; 2022, D011S020R001.
[93] Group CM. User's guide GEM, advanced compositional reservoir simulator (version 2020). computer modeling group ltd, calgary. Computer Modeling Group; 2020, URL https://www.cmgl.ca/gem.
[94] Farajzadeh R, Ranganathan P, Zitha PLJ, Bruining J. The effect of heterogeneity on the character of density-driven natural convection of CO2 overlying a brine layer. Adv Water Resour 2011;34(3):327–39. http://dx.doi.org/10.1016/j.advwatres.2010.12.012, URL https://www.sciencedirect.com/science/article/pii/S0309170810002411.
[95] Tchelepi H, Orr F. Interaction of viscous fingering, permeability heterogeneity, and gravity segregation in three dimensions. SPE Res Eng 1994;9(04):266–71.
[96] Araktingi UG, Orr F. Viscous fingering in heterogeneous porous media. SPE Adv Technol Ser 1993;1(01):71–80.
[97] Blackwell R, Rayne J, Terry W. Factors influencing the efficiency of miscible displacement. Trans AIME 1959;217(01):1–8.
[98] Yang K, Kobeissi S, Ling N, Li M, Esteban L, May EF, et al. Measurement of hydrogen dispersion in rock cores using benchtop NMR. Int J Hydrogen Energy 2023.
[99] Hughes TJ, Honari A, Graham BF, Chauhan AS, Johns ML, May EF. CO2 sequestration for enhanced gas recovery: New measurements of supercritical CO2–CH4 dispersion in porous media and a review of recent research. Int J Greenh Gas Control 2012;9:457–68.